1  **High-precision atmospheric oxygen measurement comparisons between a newly built**

2  **CRDS analyzer and existing measurement techniques**

4  Tesfaye A. Berhanu[1,2], John Hoffnagle[2], Chris Rella[2], David Kimhak[2], Peter Nyfeler[1], Markus

5  Leuenberger[1]

6  [1]*Climate and Environmental Physics, Physics Institute and Oeschger Centre for Climate Change Research,*

7  *University of Bern, Bern, Switzerland*

8  [2]*Picarro Inc., 3105 Patrick Henry Drive, Santa Clara, CA, USA*

10  **Abstract**

11  Carbon dioxide and oxygen are tightly coupled in land-biospheres $CO_2$ - $O_2$ exchange

12  processes, while they are not coupled in oceanic exchange. For this reason, atmospheric

13  oxygen measurements can be used to constrain the global carbon cycle, especially oceanic

14  uptake. However, accurately quantifying the small (~1-100 ppm) variations in $O_2$ is

15  analytically challenging due to the very large atmospheric background which constitutes

16  about 20.9 % (~209500 ppm) of atmospheric air. Here we present a detailed description of the

17  analyzer and its operating principles as well as comprehensive laboratory and field studies for

18  a newly developed high-precision oxygen mixing ratio and isotopic composition analyzer

19  (Picarro G-2207) that is based on cavity ring-down spectroscopy (CRDS). From the

20  laboratory tests, we have calculated a short-term precision (standard error of one-minute $O_2$

21  mixing ratio measurements) of < 1 ppm for this analyzer based on measurements of eight

22  standard gases analyzed for two hours consecutively. In contrast to the currently existing

23  techniques, the instrument has an excellent long-term stability and therefore a calibration

24  every 12 hours is sufficient to get an overall uncertainty of < 5 ppm. Measurements of

25 ambient air were also conducted at the High-Altitude Research Station, Jungfraujoch and the

26 Beromünster tall tower in Switzerland. At both sites, we observed opposing and diurnally

27 varying $CO_2$ and $O_2$ profiles due to different processes such as combustion, photosynthesis

28 and respiration. Based on the combined measurements at Beromünster tower, we determined

29 height dependent $O_2$:$CO_2$ oxidation ratios varying between -0.98 to -1.60 , which increase

30 with the height of the tower inlet, possibly due to different source contribution such as natural

31 gas combustion with high oxidation ratio and biological processes which are at the lower end.

## 1. Introduction

33 Atmospheric oxygen comprises about 20.9 % of the global atmosphere and in the past decade

34 its concentration decreased at a rate of ~ 20 per meg $yr^{-1}$ (Keeling and Manning, 2014) mainly

35 associated with the increase in fossil fuel combustion. Measurements of atmospheric $O_2$ are

36 reported as the ratio to the $N_2$ concentration and expressed as $\delta(O_2/N_2)$ because the variations

37 in the concentrations of other atmospheric gases such as $CO_2$ can influence the $O_2$ partial

38 pressure while this ratio is insensitive to these changes in other gases. Atmospheric $O_2$ is

39 commonly expressed in units of per meg due to its small variability with respect to a large

40 background, where

$$41 \qquad \delta\left(\frac{O_2}{N_2}\right)(per\ meg) = \left(\frac{(\frac{O_2}{N_2})sample}{(\frac{O_2}{N_2})reference} - 1\right).10^6 \qquad\qquad (1)$$

42 Note that under the assumption the atmospheric $N_2$ content is constant (i.e. $N_{2sample}$ equals

43 $N_{2reference}$), we convert relative changes in oxygen given in per meg following equation 1 to

44 oxygen changes in parts per million (equivalent to micromol/mol) by multiplying by the $O_2$

45 mole fraction ($O_{2reference}$) expressed as 209500 ppm.  (the $O_2$ mole fraction of atmospheric air)

46 (Machta and Hughes, 1970). Hence 1 ppm corresponds approximately to 4.8 per meg, or 1 per

47 meg to 1/4.8 ($209500/10^6$) ppm.

48   In contrast to $O_2$, the global average atmospheric $CO_2$ mixing ratio increased to 405.0 ppm

49   averaged over 2017  since its preindustrial value of 280 ppm (Le Quéré et al., 2017). As the

50   variability of atmospheric oxygen is directly linked to the carbon cycle, both its short and

51   long-term observations can be used to better constrain the carbon cycle. For example, since

52   first suggested by Keeling and Shertz (1992) the long-term trends derived from concurrent

53   measurements of atmospheric $CO_2$ and $O_2$ have been widely used to quantify the partitioning

54   of atmospheric $CO_2$ between the land-biosphere and oceanic sinks (Battle et al., 2000; Goto et

55   al., 2017; Manning and Keeling, 2006; Valentino et al., 2008). This method hinges on the

56   linear coupling between $CO_2$ and $O_2$ with an oxidation ratio (OR, defined as the

57   stoichiometric ratio of exchange during various process such as photosynthesis and respiration

58   expressed using α) of 1.1 for the terrestrial biosphere photosynthesis-respiration processes

59   ($α_b$) and 1.4 for fossil fuel combustion ($α_f$) while they are decoupled for oceanic processes ($α_o$

60   = 0). Meanwhile, the short-term variability in atmospheric oxygen can be used to estimate

61   marine biological productivity and air-sea gas exchange (Keeling et al., 1998; Nevison et al.,

62   2012). However, the accuracy of these estimates is primarily linked to the accuracy and

63   precision of atmospheric $O_2$ measurements and the assumed ORs for the different processes

64   which are highly variable in contrast to atmospheric $CO_2$ that can be well measured within the

65   precision guidelines set by the Global Atmospheric Watch (GAW) (± 0.1 ppm for the

66   northern hemisphere).

67       Currently there are several, mostly custom built techniques that can measure

68   atmospheric $O_2$ variations as oxygen concentration based on interferometric, paramagnetic,

69   UV absorption and fuel cell technology (Keeling, 1988a; Manning et al., 1999; Stephens et

70   al., 2007) or as $O_2/N_2$ ratios to account for the large background effect using gas

71   chromatography with thermal conductivity detector (GC-TCD) or gas chromatography

coupled to mass spectrometry (GC-MS) (Bender et al., 1994; Tohjima, 2000). Despite the fact that these techniques have been used for more than two decades, accurate quantification of atmospheric oxygen variability remains challenging primarily because the small ppm-level atmospheric oxygen signal rides on a $\sim$ 210,000 ppm background, which places stringent requirements on the precision and drift of the analysis methods especially for continuous monitoring(note that the GAW recommendation for the measurement precision of $O_2/N_2$ is 2 per meg). The techniques listed above struggle to routinely achieve the necessary performance for various reasons, including i) instability over time that requires frequent measurement interruption for calibration, ii) measurement bias with ambient and sample temperature and/or pressure, and/or iii) systematic errors in the measurement due to other atmospheric species. Further, some techniques require the use of consumables and rely on high vacuum, which complicates field deployment.

In this manuscript we describe a new high precision oxygen concentration and isotopic composition analyzer by Picarro Inc., Santa Clara, USA (G-2207) based on CRDS technology. Here, we will introduce the analyzer design principles in details, describe the unique features of the analyzer and evaluate its performance based on various independent laboratory and field tests by comparing it with currently existing techniques. Then, we will present and interpret our observations based on field measurements. Finally, we will conclude its overall performance and provide recommendations and possible improvements.

**2. Analyzer design principles**

The analyzer described here is derived from the Picarro G2000 series of CRDS analyzers. The basic elements have been described elsewhere (Crosson, 2008; Martin et al., 2016; Steig et al., 2014): briefly, the instrument is built around a high-finesse, traveling-wave optical cavity, which is coupled to either of two single-frequency Distributed FeedBack-

96   stabilized semiconductor lasers. One cavity mirror is mounted on a piezoelectric translator

97   (PZT) to allow fine tuning of the cavity resonance frequencies. A semiconductor optical

98   amplifier between the laser sources and the cavity boosts the laser power and serves as a fast-

99   optical switch. The cavity body is constructed of invar and enclosed in a temperature

100  stabilized box (T = 45° C, stabilized to approximately 0.01 °C) for dimensional and

101  spectroscopic stability. A vacuum pump pulls the gas to be sampled through the cavity and a

102  proportional valve between the cavity and the pump maintains the sample pressure in the

103  cavity at a value of 340 hPa, with variations on the order of 1 Pa. The instrument has a

104  wavelength monitor, based upon measurements of interference fringes from a solid etalon,

105  which is used to control the laser wavelength by adjusting the laser temperature and current.

106  The wavelength monitor is a fiber-coupled device located between the laser and the cavity. A

107  fraction of the beam from the input fiber is collected using a beam splitter for the wavelength

108  measurement and the remaining power is collected in the output fiber. A high-speed

109  photodiode monitors the optical power emerging from the cavity. The instrument's data

110  acquisition system is used to sweep the laser frequency over the spectral feature to be

111  measured, modulates the laser output to initiate ring-downs, and fits the ring-down signal to

112  an exponential function to generate a spectrogram of optical loss versus laser frequency. For

113  this instrument the empty cavity ring-down time constant is about 39 $\mu$s. Subsequent program

114  modules compare the measured loss spectrum to a spectral model, using non-linear least-

115  squares fitting (Press et al., 1986) to find the best-fit model parameters and thereby obtain a

116  quantitative measure of the absorption due to the target molecule, and finally apply a

117  calibration factor to the optical absorption to deduce the molecular concentration. When

118  operating in its normal gas analysis mode, the instrument acquires about 200-300 ring-downs

119 per second and achieves a noise equivalent absorption of typically about $10^{-11}$ cm$^{-1}$ Hz$^{-1/2}$,

120 with some variation between instruments.

121      The primary goal when designing this analyzer was to measure the molecular oxygen

122 concentration with few-per-meg level precision and stability. In this context operational

123 stability is as important as signal-to-noise. Our experience has been that the most stable

124 operation of the analyzer is achieved when the optical phase length of the cavity is held as

125 nearly constant as possible. In this case the free spectral range (FSR, 0.0206 cm$^{-1}$) of the

126 temperature stabilized, invar ring-down cavity provides a better optical frequency standard

127 than the etalon-based wavelength monitor, which in turn allows more consistent

128 measurements of absorption line width and integrated absorption line intensity (Steig et al.,

129 2014). For a small, field-deployable instrument, it is not practical to stabilize the absolute

130 frequencies of the cavity modes to an optical frequency standard (Hodges et al., 2004) but the

131 oxygen lines themselves, under conditions of constant temperature and pressure, provide an

132 adequate frequency reference. The oxygen spectrum was also used to calibrate the FSR, by

133 comparing a wide (approximately 10 cm$^{-1}$) FSR-spaced spectrum with the Hitran database

134 (Rothman et al., 2013).

135      To determine molecular oxygen concentration, the analyzer measures absorption of the

136 Q13Q13 component of the $a^1\Delta_g \leftarrow X^3\Sigma_g^-$ band, at 7878.805547 cm$^{-1}$, according to the latest

137 edition of Hitran (Gordon et al., 2017). This is one of the strongest near-infrared lines of

138 oxygen, well separated from other oxygen lines, and reasonably free of spectral interference

139 from water, carbon dioxide, methane, and other constituents of clean air. The spectral model

140 for this line was developed using reference spectra of clean, dry, synthetic air that were

141 acquired with the same hardware as in the field-deployable analyzer, but with special-purpose

142 software that allows it to operate as a more general spectrometer.

Recently, considerable work has been done to advance the understanding of spectral line shapes and to define functional representations that better describe the processes that determine spectral line shapes than does the Voigt model (Hartmann et al., 2008; Tennyson et al., 2014, Tran et al., 2019). Line shape studies have been published for the 1.27 μm band of $O_2$ (Fleisher et al., 2015; Lamouroux et al., 2014), though not to our knowledge for the Q branch. The apparatus used here is not capable of spectroscopic studies of comparable precision; the absolute temperature and pressure monitoring and especially the frequency metrology are far too crude for that purpose. Our goal is merely to define a simple model of the Q13Q13 line that is adequate for least-squares retrievals of the $O_2$ absorption under the limited range of conditions (stabilized temperature and pressure) that the operational analyzer experiences in the field. The CRDS analyzers use the Galatry function (Varghese and Hanson, 1984), which is distinctly better than the Voigt and still easily and quickly evaluated for line shape modeling. Ultimately, the usefulness of the spectral model is to be evaluated by the precision and stability of the $O_2$ measurements when compared with established techniques. For spectral model development, this spectrometer has the drawback that the cavity FSR, is too large to reveal much detail of the absorption line shape, even with the simplifying assumption of a Galatry line shape. We therefore acquired a set of four interleaved spectra, with the PZT-actuated mirror moved to offset the cavity modes of the individual FSR-spaced spectra by one-fourth of an FSR. The precise offsets were determined from fits to the strong and well-isolated $O_2$ lines in the spectra. From the consistency of the fitted line centers, we estimate that the positioning of the interleaved spectra was accurate to approximately 10 MHz. The spectrum of the Q13Q13 line acquired in this manner is shown in Figure 1, together with the best-fit Galatry function. It stands out that the residuals are largely odd in detuning from the line center: this shows the limitations of the Galatry model in this case,

167    since the Galatry function is purely even about the line center. The shape of the absorption

168    line in this model is specified by two dimensionless parameters: the collisional broadening

169    parameter

170    $y = \gamma/\sigma_D$ (2)

171    and the collisional narrowing parameter

172    $z = \beta/\sigma_D$ (3)

173    where $\gamma$ is the frequency of broadening transitions, $\beta$ is the velocity change collision rate, and

174    $\sigma_D$ is the 1/e Doppler half-width of the transition, given by

175    $\sigma_D = \nu_0(2k_BT/Mc^2)^{1/2}$ (4)

176    where $\nu_0$ is the transition frequency, $k_B$ is Boltzmann's constant (J. $K^{-1}$), T is the sample

177    temperature (K), M is the molecular mass (amu), and c is the speed of light (m/s). Figure 2

178    shows the values of y and z obtained from spectra acquired in the same way as Figure 1, as a

179    function of cavity pressure. The values depend linearly on pressure, as expected from the

180    Galatry model, but the unconstrained linear fits do not go precisely through the origin. It is

181    not clear whether this represents a breakdown of the Galatry model or simply reflects the

182    limited quality of the data set. The slope of y can be converted to an air-broadened collisional

183    width $\gamma_{air} = 0.0442$ cm$^{-1}$/atm, which agrees with the Hitran value of 0.0460 cm$^{-1}$/atm (Gordon

184    et al., 2016) to within the uncertainty estimate stated by Hitran (uncertainty code 4 for $\gamma_{air}$

185    corresponding to 10% --20% relative uncertainty). The slope of z can be interpreted in terms of

186    the optical diffusion coefficient (Fleisher et al., 2015), yielding D = 0.285 cm$^2$ s$^{-1}$, compared

187    to the literature value of 0.233 cm$^2$ s$^{-1}$ for $O_2$ in air at 45 °C (Marrero and Mason, 1972).

188    Although the anticipated use of the analyzer is for ambient air samples having a very small

189    range of $O_2$ concentrations, we did investigate the variation of the line shape in binary

190    mixtures of $O_2$ and $N_2$ shown in Figure 3. The error bars are taken from the output of the

191  Levenberg-Marquardt fitting routine (Press et al., 1992). The dependence of the collisional

192  broadening parameter z on $O_2$ mole fraction was considered too small to be significant, but

193  the variation in y was used in the subsequent analysis of the air samples.  Note that Wójtewicz

194  et al. (Wójtewicz et al., 2014) also found collisional broadening coefficients for nitrogen to be

195  slightly larger than for oxygen in measurements of one $O_2$ line in the B-band.

196  The primary goal in designing the analyzer was to achieve high enough precision to

197  make meaningful measurements of $O_2$ in clean atmospheric samples. Although the current

198  best practice for such high-precision measurements is to work with dried samples, we decided

199  to include high precision measurements of water vapor. There were two reasons for this

200  decision: one is to serve as a monitor for residual water vapor, which is difficult to remove

201  completely from the ring-down cavity and associated sample handling hardware, and the

202  second and more ambitious reason was to see how well the effect of water vapor could be

203  corrected for measurements of undried ambient air. While it was considered unlikely that

204  measurements of undried air could compete in accuracy with those of dried air, it might be

205  possible to correct for water vapor well enough to enable useful measurements in some

206  circumstances without the expense and inconvenience of drying the sample.  For this purpose,

207  a second laser was added, which probes the $7_{1,6} \rightarrow 8_{4,5}$ component of the $2v_3$ band of water

208  vapor, at of 7816.75210 cm$^{-1}$ (Gordon et al., 2017).  The Galatry model was used to fit spectra

209  of synthetic air humidified to various levels of water vapor concentration. These fits also

210  included two other nearby, very weak water lines, with intensities less than 1% of the strong

211  transition, in order that their absorption should not perturb the line shape of the main

212  transition.  Results for the shape of the 7816.75210 cm$^{-1}$ line are shown in Figure 4. At the

213  level that we can measure, only the y-parameter has a meaningful variation with water

214  concentration. From the linear fit one obtains a pressure broadening coefficient for air, $\gamma_{air}$ =

215    0.0752 cm$^{-1}$/atm, in reasonable agreement with the Hitran value $\gamma_{air}$ = 0.0787 cm$^{-1}$/atm

216    (Gordon et al., 2017), and a self-broadening coefficient $\gamma_{self}$ = 0.413 cm$^{-1}$/atm, to be compared

217    with the Hitran value $\gamma_{self}$ = 0.366 cm$^{-1}$/atm. Since the uncertainty estimate for the Hitran

218    values is 10 % to 20 %, this level of agreement seems reasonable.

219          We also looked at absorption from water near the Q13Q13 absorption line of $O_2$.

220    These spectra were measured in a background of pure nitrogen to reveal the very weak lines

221    interfering with the $O_2$ measurement. Without the strong $O_2$ lines, it was impossible to

222    interleave FSR-spaced spectra, so in this case the frequency axis comes from the analyzer's

223    wavelength monitor. The upper panel of Figure 5 shows the spectrum of saturated water vapor

224    in nitrogen, together with a fit to a Voigt model of the molecular lines. The measurement was

225    made at a pressure of 340 hPa and temperature of 45° C. The main features are the Q13Q13 line

226    from trace contamination of oxygen in the sample and several lines that arise from normal water

227    ($^1H_2^{16}O$) and deuterated water ($^1H^2H^{16}O$ also abbreviated HDO). The lower panel of Figure 5 shows

228    the lines tabulated in Hitran. Immediately after the data in Figure 5 were acquired,

229    measurements were also made at 7816.85210 cm$^{-1}$, to establish the relationship between the

230    absorption strengths in the two spectral regions. The relative intensities of the $H_2O$ and HDO

231    lines change with variations in the isotopic composition of the water, but fortunately the direct

232    interference with the oxygen Q13Q13 lines comes entirely from the $H_2O$ isotopologue, with

233    the strongest HDO line being separated by approximately 8 line widths (FWHM) from the

234    Q13Q13 line.  Hitran simulations for molecules other than water that are expected to be

235    present in clean, ambient air indicate that direct interference with the Q13Q13 line should be

236    negligible at the level of precision considered here. In the case of $CO_2$, the dilution of oxygen

237    due to 400 ppm of $CO_2$ is significant, and larger than any direct spectral interference.

238    Finally, we investigated the influence of water vapor on the shape of the $O_2$ Q13Q13

239    line. Switching between the two lasers sources, we acquired FSR-spaced spectra of

240    humidified synthetic air, alternately covering the 7817 $cm^{-1}$ and 7878 $cm^{-1}$ regions.  Individual

241    spectra were acquired in less than 2 s, so changes in water vapor concentration between

242    spectra were small. These spectra, with frequency resolution of 0.0206 $cm^{-1}$, were analyzed by

243    nonlinear least-squares fitting with the following spectral models:  the 7817 $cm^{-1}$ spectra were

244    modeled as the sum of an empty-cavity baseline having an adjustable offset level and slope

245    and the water spectrum is modeled with three peaks: one strong line and two weak perturbers.

246    The molecular absorption of the main peak was expressed as an adjustable amplitude, $A_w$,

247    multiplying a dimensionless, area-normalized Galatry function (Varghese and Hanson, 1984).

248    The weak perturbers were modeled by Voigt profiles with amplitudes and line widths that

249    were constrained to be in fixed proportions to the strong line, and therefore added no new

250    degrees of freedom to the fitting procedure. Since the amplitude $A_w$ multiplies an area-

251    normalized shape function, it is essentially equivalent to the area of the absorption line, to the

252    extent that the Galatry model provides a valid description of the line shape. The Doppler

253    width of the Galatry function was fixed based on the measured cell temperature, the y-

254    parameter was allowed to vary, and the z-parameter was constrained to be proportional to y,

255    based on measurements summarized in Figure 2.  In addition, the center frequency of the

256    Galatry function was adjusted to match the data set, giving a total of five free parameters for

257    this fit. The 7878 $cm^{-1}$ spectra were modeled with an adjustable baseline offset and slope and

258    molecular absorption amplitude, $A_{O2}$, describing the Q13Q13 $O_2$ line.  Here, too, the y-

259    parameter and line center position of the $O_2$ lines were allowed to adjust, and the z-parameter

260    was constrained to be proportional to y. The weak water lines interfering with oxygen

261    absorption were included in the model, but with no additional free parameters; rather the

262    amplitudes were preset based on the measured water absorption at 7817 cm$^{-1}$ and the

263    previously determined amplitude relationships between the water lines. This procedure does

264    not account for variations in HDO abundance, which may introduce some systematic error

265    into the water vapor correction for samples of unusual isotopic composition, but it should

266    accurately model the most important lines that interfere with the oxygen measurement.

267    Collisional broadening of the Q13Q13 O$_2$ line by water vapor is shown in Figure 6.  From the

268    linear fit one obtains a coefficient for collisional broadening of the Q13Q13 line by water

269    vapor of $\gamma_{water}$ = 0.0442 cm$^{-1}$/atm at 45 °C. Recently, parameters describing broadening of

270    oxygen lines by water vapor, obtained by empirical modeling of selected experimental

271    data, were added to the Hitran data base (Tan et al., In review). The new Hitran entries predict

272    a value of 0.0486 cm-1/atm at 45 °C, which is in agreement with our measurement within the

273    5-10% uncertainty attributed by Hitran to the broadening parameter. The alternating

274    measurements at 7817 cm$^{-1}$ and 7878 cm$^{-1}$ also calibrated the relationship between water mole

275    fraction and the absorption at 7817 cm$^{-1}$, using a dilution analysis described by Filges et al.

276    (2018), who showed that the results obtained this way agree well with water vapor fractions

277    measured with a conventional hygrometer. Figure 7 shows the measured amplitudes of the

278    water and oxygen lines for samples of variable humidity. Since the air came from a tank of

279    constant composition, the oxygen concentration changes due to dilution of oxygen when

280    water is added. Assuming that this is the sole cause of the change in measured absorption,

281    since the line shapes were being constantly adjusted to account for changes in collisional

282    broadening, it is straightforward to deduce the relation between the water fraction and the

283    absorption amplitude. This calibration was used to generate the water fraction axes in Figures

284    4 and 6. We note that we did not take particular care to control or measure the quantity of

285    dissolved gases, especially oxygen and carbon dioxide, in the water used for this experiment.

While these gases would not significantly affect the water calibration, they may affect the water vapor correction of the oxygen measurement at the ppm level. More work needs to be done to investigate the water vapor correction of the oxygen measurement.

The observations described above were used to design a method to measure oxygen concentration in ambient air. Gas from the inlet to the analyzer is drawn through the cavity at a rate of about 100 sccm (standard cubic centimeter per minute) and the conditions in the cavity are held stable at 340 hPa and 45°C. In its analysis mode the analyzer alternately measures ring-downs in the 7817 $cm^{-1}$ and 7878 $cm^{-1}$ regions. At 7878 $cm^{-1}$ measurements are made at 11 different frequencies, spaced by one FSR of the cavity and centered at the peak of the Q13Q13 line. Multiple ring-down measurements are made to improve the precision of the loss determination, with a total of 305 ring-downs allocated to one spectrum. In the 7817 $cm^{-1}$ region measurements are also made at 11 distinct frequencies at FSR spacings. Only 35 ring-downs are allocated to this spectral region, since the measurement of $O_2$ is much more important than water vapor. The data sets are analysed using a Levenberg-Marquardt fitting routine, which adjusts five free parameters in each region to find the best agreement to a spectral model based on Galatry line shapes, as described above. One of the outputs of the 7878 $cm^{-1}$ fit is the frequency offset of the FSR grid from the center of the Q13Q13 line. This information is used to adjust the position of the PZT actuated mirror to keep the measurements centered on the line, effectively stabilizing the optical path length of the cavity to the frequency of the $O_2$ line. The reported water fraction is obtained by multiplying the fitted amplitude of the water line by a calibration constant derived from the dilution experiment as explained above. For the $O_2$ fraction a slightly more complicated procedure is followed. It was observed that the least-squares fitting of the data gives highly correlated results for the amplitude of the absorption line and the line width parameter y. The correlation

310   may be due in part to covariance of the fitted amplitude (proportional to line area) and line

311   width (Press et al., 1992) and it may also have a contribution from pressure variations that the

312   pressure sensor is unable to detect.  The ratio $A_{O2}/y$ can be determined from the fit much more

313   precisely than $A_{O2}$ alone and so gives a more sensitive measurement of molecular absorption.

314   It also has the advantage of being independent of sample pressure, to the extent that the

315   Galatry model applies (Figure 2).  However, using the ratio $A_{O2}/y$ as a metric for absorption

316   adds more complications if measurements are to be made over a range of $O_2$ and water

317   concentrations, because the $O_2/ N_2$ ratio and the water concentration affect the line width

318   independently of pressure and $O_2$ concentration alone. To minimize systematic errors due to

319   these broadening effects, we define a nominal y-parameter based on the measured amplitudes

320   of the $O_2$ and water lines and the line broadening dependences shown in Figures 3 and 4. The

321   measured ratio $A_{O2}/y$ is multiplied by the nominal y to obtain a quantity that is ideally

322   independent of pressure and water concentration, and this is the quantity that is multiplied by

323   a calibration constant to give the reported $O_2$ fraction. In addition, a dry mole fraction is

324   reported for $O_2$, defined as the directly measured mole fraction corrected for water dilution.

325        The main goal in developing this instrument was to make high precision

326   measurements of $O_2$ mole fraction, based on absorption by the dominant $^{16}O_2$ isotopologue.

327   The absorption lines of the rarer isotopologues are also present nearby, so a mode of operation

328   was included in which one laser is scanned over neighboring lines of $^{16}O_2$ and $^{16}O^{18}O$ and the

329   ratio of amplitudes is used to derive an isotopic ratio, reported in the usual delta notation. In

330   this case the operating pressure was reduced to 160 hPa to improve the resolution of the

331   nearby lines. The lines measured were the Q3Q3 line of $^{16}O_2$, at 7882.18670 cm$^{-1}$, and the

332   Q9Q9 line of $^{16}O^{18}O$, at 7882.050155 cm$^{-1}$. The measurement procedure is very much like

333   that for the $O_2$ fraction measurement, so it will not be described in detail, only the main

334 differences will be noted. One is that in determining an isotopic ratio, normalizing absorption

335 amplitudes by line widths does not provide any advantage, instead we simply take the ratio of

336 amplitudes to compute delta. Although the Q9Q9 line and its neighbor Q8Q8 are the strongest

337 ones in this band, absorption by $^{16}O^{18}O$ is still very weak, only about $5\times10^{-9}$ cm$^{-1}$ at the line

338 center under the conditions we used. The signal-to-noise that can be achieved with this

339 analyzer is not adequate to determine both the amplitude and the width of the $^{16}O^{18}O$ line with

340 useful precision, so in the fitting step the y-parameter of the $^{16}O^{18}O$ line is constrained to be a

341 constant factor times the fitted y-parameter for the $^{16}O_2$ line. Additionally, because of the

342 weakness of the rare isotopologue absorption, the majority of ring-downs in each spectrum is

343 devoted to measuring $^{16}O^{18}O$ i.e. 232 ring-downs in each spectrum versus only 40 for $^{16}O_2$.

344 This implies that the mole fraction measurement in the isotopic mode is much less precise

345 than when the analyzer measures the Q13Q13 line alone.

346 **3. Results and Discussions**

347 **3.1. Laboratory tests at Picarro, Santa Clara**

348 3.1.1. Temperature and pressure sensitivity

349    One set of tests was done to determine how well the goal was met of minimizing the

350 susceptibility of the concentration measurements to noise or drift of the sample temperature

351 and pressure. For these tests the analyzer sampled dry synthetic air from a tank and the

352 temperature and pressure setpoints of the cavity were adjusted upward and downward from

353 the nominal values, to obtain an estimate of the differential response. We express the

354 sensitivity to experimental conditions in relative form, that is the derivative with respect to

355 temperature or pressure divided by the signal under nominal conditions.

356    From these experiments, we determined a temperature sensitivity of $-2.1\times10^{-4}$ K$^{-1}$ and

357 a pressure sensitivity of $+9.8\times10^{-6}$ hPa$^{-1}$. The temperature sensitivity is somewhat larger than

358  expected based on a calculation using Hitran data to estimate the temperature dependences of

359  all the quantities that go into the measured absorption of the Q13Q13 line. The pressure

360  sensitivity is strikingly small, indicating a good cancelation of the pressure dependence of

361  absorption amplitude and line width. Both temperature and pressure sensitivities are small

362  enough to have a negligible effect on short-term precision of measurements made with the

363  stabilized ring-down cavity, though long-term drifts in the sensors are always a matter of

364  concern.

365  3.1.2. Measurement precision and drift

366      Measurement precision was evaluated by analyzing synthetic air containing nominal

367  atmospheric concentrations of $CO_2$ and $CH_4$ from an aluminum Luxfer cylinder over a period

368  of several days. The tank, oriented horizontally and thermally insulated (though not

369  controlled), was connected directly to the instrument (S/N TADS2001) with a 2-stage

370  pressure regulator and stainless-steel tubing with an additional orifice to about 55 sccm. For

371  the isotopic mode of operation, the precision of the measurement was also tested by making

372  repeated measurements from a tank of clean, dry synthetic air.

373      Figure 8 shows the time series of the precision test data, displaying the reported

374  oxygen concentration, the height of the oxygen absorption peak, the width of the oxygen

375  absorption peak and the ambient temperature. The residual error of the analyzer, although

376  small, is nevertheless significant given the stringent targets set forth by the WMO-GAW

377  program. Possible sources of error include: temperature drifts due to sensor drift or gradients;

378  pressure errors due to sensor drift; optical artifacts such as parasitic reflections, higher order

379  cavity mode excitation, and/or loss nonlinearity that can distort the reported oxygen spectrum.

380  More work is required to identify and eliminate these small drifts.

The Allan standard deviation of the reported $O_2$ fraction is shown in the Allan-Werle plot in Figure 9. The ordinate on this plot is the square root of the Allan variance of reported mole fraction, so 1 ppm in these units corresponds to about 5 per meg in the ratio of $O_2/N_2$. The precision of averaged measurements improves as $\tau^{-1/2}$ for approximately 5000 s and reaches 1 ppm in less than 10 minutes and remains below 1 ppm for time scales on the order of about 1 hour ($\tau$ is the averaging time which is the abscissa of the Allan-Werle plot).

Figure 10 shows the precision of $\delta(^{18}O)$ (uncalibrated) derived from the ratio of lines measured at 7882 cm$^{-1}$. Because of the weak signal from the $^{16}O^{18}O$ line, it is necessary to average for more than 20 seconds or more to achieve 1‰ precision on the isotopic ratio. As for the concentration measurement, averaging improves the measurement precision for time scales up to about 1 hour.

**3.2. Laboratory measurements at the University of Bern**

3.2.1. Measurements of standard gases

The performance of the instrument was tested by analyzing eight standard gases with precisely known $CO_2$ and $O_2$ compositions (Table 1) using the CRDS analyzer and comparing it to parallel measurements with a paramagnetic oxygen sensor (PM1155 oxygen transducer, Servomex Ltd, UK) embedded to a commercially available fuel cell oxygen analyzer (OXZILLA II, Sable Systems International, USA) (Sturm et al., 2006) as well as with an isotope ratio mass spectrometer (IRMS, Finnigan Delta$^{Plus}$XP). The design of the measurement set-up is shown in Figure 11. Standard gases were directly connected to the pressure controlling unit, and a multi-port valve (V2) was used to select among the standard gases. Flow from each cylinder was adjusted to about 120 sccm which was eventually directed to a selection valve (V1), allowing switching between ambient air and standard gases. Flow towards and out of the fuel cell analyzer was controlled by the pressure controlling unit.

405    The $O_2$ mixing ratio of this incoming gas was first measured on the Paramagnetic $O_2$ sensor

406    and then directed towards a non-dispersive infrared analyzer (NDIR) (Li-7000, LICOR, USA)

407    for measuring $CO_2$ and $H_2O$. The outflow from this analyzer (100 sccm) returns to the

408    pressure controlling unit and was eventually divided between the CRDS analyzer (which uses

409    about 75-80 sccm) and the IRMS (~ 20 sccm) via a Tee-junction. Each cylinder was measured

410    for two hours in each system controlled by a LabView program.

411        First, we investigated the influence of this Tee-junction, which splits the gas flow

412    between the CRDS and the IRMS, on the measured $O_2$ values. Manning (2001) showed that

413    the fractionation of $O_2$ in the presence of a Tee-Junction is strongly dependent on the splitting

414    ratios as well as temperature and pressure gradients. Hence, we measured and compared the

415    $O_2$ mixing ratios of two standard gases (CA07045 and CA060943) in two cases: i) in the

416    presence of a Tee-junction with different CRDS to IRMS splitting ratios and ii) without a

417    Tee-junction so that all gas flow is directed towards the CRDS analyzer. The splitting ratios in

418    these test experiments vary from 1:1 to 1:100, and reversed to change the major flow direction

419    either to the CRDS or the IRMS. Note that the experimental condition in this manuscript is

420    with a 4:1 splitting ratio (i.e. ~ 80 sccm towards the CRDS analyzer and ~ 20 sccm towards

421    the IRMS).

422        In the cases of the smaller splitting ratios (1:1, 1:4 and 4:1), which are relevant for the

423    results presented in this study, only minor differences in the measured $O_2$ mixing ratios were

424    observed when compared to case ii (i.e. without a Tee-junction). For these two cylinders

425    measured, the average differences in these cases were about 0.5 ppm, calculated as the mean

426    of the differences in the raw $O_2$ measurements of the last 60 seconds. The negligible

427    fractionation can indeed be the result of smaller splitting ratios while strong influence is

428    usually expected in case of larger splitting ratios (Stephens et al., 2007). For higher splitting

429    ratios, the result seems inconclusive without any dependence on the ratios due to the strong

430    decline in the cylinder temperature (specifically at the pressure gauge) caused by higher flow

431    to achieve the higher splitting ratios (as high as 1:100). Hence, these tests need to be

432    conducted in a temperature-controlled condition and the results could not be discussed in this

433    manuscript.

434         Figure 12 shows the standard gas measurements for the seven cylinders with known

435    $CO_2$ and $O_2$ mixing ratios (Table 1) using both the CRDS and the Paramagnetic analyzers.

436    Standard eight, which has too high $O_2$, is not shown in the figure as the figure is zoomed-in to

437    better illustrate the change in $O_2$ for the remaining cylinders. While the first five cylinders

438    contain $O_2$ and $CO_2$ mole fractions comparable to ambient air values, standards 6 & 8 had

439    either very low or very high $O_2$, respectively. In addition, standards 6 and 7 have very low and

440    very high $CO_2$ mixing ratios. Note that due to its very high $CO_2$ content ($\sim$ 2700 ppm),

441    standard 7 was not measured on the IRMS and hence the $O_2$ mixing ratio is unknown. The

442    measured mixing ratios for the six standard gases measured with the two systems are in very

443    good agreement while cylinder 7 showed an opposing signal for the two analyzers compared

444    to standard 6 (Figure 12). While the Paramagnetic analyzer showed a higher $O_2$ mixing ratio,

445    the values from the CRDS analyzer are lower in $O_2$. This can be associated with the very high

446    $CO_2$ mixing ratio in standard 7, which leads to a strong dilution effect in the CRDS analyzer

447    as it does not include any correction function for dilution effect from $CO_2$. However, such

448    high $CO_2$ mixing ratios may not be that important for most atmospheric research. Yet, it

449    should be considered to include a parallel $CO_2$ mixing ratios measurement to the instrument

450    as it will further improve the accuracy. This would be especially important for biological or

451    physiological studies where a wide range of $CO_2$ and $O_2$ concentrations must be expected.

452     The measurement precision of the CRDS analyzer was calculated as the standard error

453     of the mean i.e. the standard deviation (1-σ) of the last 1-minute raw measurements divided

454     by the square root of the number of measurements (n = 60), and for all these cylinders the

455     values are usually between 0.5 ppm to 0.7 ppm. For parallel measurements of these cylinders

456     using a Paramagnetic analyzer, we obtained a precision of about 1 ppm, calculated exactly the

457     same way.

458     We also made a correlation plot to see which of the two instruments are in better

459     agreement with the assigned values based on IRMS measurements for the individual

460     cylinders. While similar correlation coefficients were observed for both analyzers, different

461     slopes were calculated (Fig. A.1). This is due to the fact that the IRMS measures the $O_2$ to $N_2$

462     ratio ($\delta(O_2/N_2)$) in per meg, while the CRDS and the Paramagnetic analyzers provide non-

463     calibrated $O_2$ mixing ratios in units of ppm and per meg, respectively. If we exclude the two

464     standard gases with the highest and lowest $O_2$ mixing ratios (standards 7 and 8) that are

465     subjected to strong dilution effects, both the slope and the $r^2$ values decrease from those

466     shown in Figure A.1. But this decrease is larger in the case of the Paramagnetic

467     measurements, implying a slightly better linearity of the CRDS analyzer.

468     Furthermore, the slope between the IRMS and CRDS $O_2$ values in Figure A1

469     corresponds to 5.78 per meg ppm$^{-1}$, significantly larger than the conversion factor of 4.78 per

470     meg ppm$^{-1}$ as derived from equation 1 assuming constant $N_2$ content. This higher slope is due

471     to dilution effect originating from any gas component change (Delta, given in ppm) on all air

472     components of air samples, which has not been corrected for the CRDS values. When

473     accounting for this dilution effect - which scales with 1/(1+Delta), the factor approaches 4.78

474     per meg ppm$^{-1}$. The scaling of dilution effects is independent on which air component is

475     changing and it affects all air components relative to their molecular fractions similarly. $O_2$

476 values on a CRDS or paramagnetic cell instrument is affected even if there is no change in $O_2$

477 or $N_2$ but only in $CO_2$ or water vapor or any other component which is present. This is in

478 contrast to measurements of O2/N2 ratios for the same case where equal ratio would be

479 measured. Major dilution influences are expected from $O_2$, $CO_2$ and $H_2O$ changes due to

480 natural exchange processes on air samples or when using artificial air-like compositions.

481 3.2.2. Measurements of ambient air

482 Ambient air measurements were conducted from the roof top of our laboratory at the

483 University of Bern to evaluate the analyzer's performance under atmospheric variability.

484 Ambient air was continuously aspirated from the inlet at the roof of the building at a flow rate

485 of ~ 250 sccm which is then dried using a cooling trap kept at -90 °C towards the switching

486 valve (V1) and measured in similar way to the standard gases as explained above. The

487 measurement values obtained here were compared with the parallel measurements by the

488 Paramagnetic sensor to test the instruments stability and accuracy.

489 Figures 13 panels a &b show the 1-minute average ambient air measurements from the

490 rooftop inlet by the Paramagnetic and the CRDS analyzers at the beginning of the testing

491 period including standard gases measured every 12-hour. While the Paramagnetic analyzer

492 seems to be stable, the CRDS analyzer showed a strong drift for an extended period. This can

493 be due to unstable conditions in the CRDS measurement system as it started operating right

494 after it was unpacked. Hence, we looked into temperature inside the instrument chassis and

495 pressure records, which were stable within the manufacturer's recommended range during this

496 period. As the CRDS analyzer incorporates a water correction function, interference from this

497 species should be well accounted. Even comparing the analyzer's parallel water

498 measurements to water measurements by the NDIR system such a drift was not observed. It

499 should be noted that the two internal standard gases which were less frequently measured

500    (every 12 hours) during this period were also drifting following similar pattern. This implies

501    that the drift is associated with the analyzer. Interestingly, this pattern can be modeled using a

502    polynomial function which can then be used to correct for the observed drift in the ambient air

503    measurements. After applying a polynomial drift correction, we were able to fully accounted

504    for the observed drift. However, the manufacturer decided to further investigate possible

505    causes of this drift. After further improvements, we obtained the first commercial analyzer in

506    September 2017 and repeated the above tests (Figure 13 c &d). No such drift was observed

507    any more in the standard gases or in ambient air measurements.

508    We believe that the optical amplifier has caused the drift in the first system and not anymore

509    included in the design of the product which produced a significant amount of broadband light

510    that could fill the cavity (albeit with a low coupling coefficient), and would ring down with a

511    different (and generally much faster) time constant that the baseline loss of the cavity.

512    However, the ringdown time on the peak of the oxygen line is just 10 microseconds, such that

513    the broadband light might have distorted the single exponential decay of the central laser

514    frequency, leading to the observed drift in the oxygen signal.  However, we were not able to

515    confirm this hypothesis.

516    3.2.3. Water correction test

517        Measurements of oxygen are reported as both wet ($O_{2,\ raw}$) and dry ($O_{2,\ dry}$) mole

518    fractions by the CRDS analyzer as it also measures water vapor in parallel at its water

519    absorption line (7817 cm$^{-1}$), and corrects for the dilution effect based on an inbuilt numerical

520    function:

521    $$O_{2,dry} = \frac{O_{2,raw}}{1-H_2O} \qquad (5)$$

522    where $H_2O$ is the measured water mole fraction.

523    The efficiency of water correction by this function was assessed in two ways: i) by comparing

524    the water vapor content in standard air measured by this analyzer with similar measurements

525    by the NDIR analyzer and ii) by comparing the oxygen mixing ratios between non-dried

526    ambient air measured and corrected for water dilution by the CRDS analyzer with dried air

527    measured using a paramagnetic analyzer.

528         Figure 14 shows the water vapor content for standard gases measured continuously for

529    two days by the CRDS and the NDIR analyzers. Note that the two data sets are manually

530    fitted to each other as the measured water values by the NDIR analyzer are not calibrated.

531    Based on this plot, the two analyzers are in very good agreement although there are small

532    differences during very dry conditions (low water content).

533         Figure 15a shows the dried ambient air water measurements in both analyzers with

534    frequent spikes due to valve switching while measuring standard gases. In the second case,

535    where the water trap was by-passed and non-dried air was allowed to the CRDS analyzer

536    keeping the dried air flow to the NDIR (Figure 15b), a clear increase in the water

537    measurements in the CRDS analyzer can be observed. Here, it should be noted that there are

538    no spikes in the water measurements of the CRDS analyzers as there are no standard gas

539    measurements in between and the inlet is directly connected to the CRDS analyzer (Figure

540    11). Figures 15c & 15d show the difference in oxygen measurements of ambient air measured

541    in both analyzers in the two cases stated above (note that the CRDS uses its built-in water

542    correction function applying Eq. 5). The measurements of the Paramagnetic analyzer were

543    scaled to ppm units by applying the correlation equation obtained from the six standard gas

544    measurements of the two analyzers (Fig. A.1). Note that the CRDS measurements were

545    corrected for the observed drift using the polynomial fit to the two standard gas measurements

546    stated above.

547     In the first period of the measurement when both analyzers measured dried ambient

548     air, the absolute differences between the 1-minute averages measured over two days by the

549     two analyzers were mostly within 15 ppm (Figure 15c) and symmetrically distributed around

550     zero (Figure 15e). However, when wet air was admitted to the CRDS analyzer and the in-built

551     water correction was applied, a stronger variability was observed in the calculated differences

552     (Figure 15d). This implies stronger short term variability in the CRDS analyzer measurement

553     values (as nothing was changed for the Paramagnetic measurement system) when wet samples

554     were analyzed. The more negative values in the differences (Figure 15f) can also be

555     associated with overestimation of the $O_2$ mixing ratios by the CRDS originating from an

556     overestimated water correction. However, detailed evaluation of the analyzer's water

557     correction function is beyond the scope of this study.

558     **3.3. Field Measurements**

559     After a series of tests at University of Bern, we conducted multiple field measurements

560     at the High Altitude Research Station Jungfraujoch and the Beromünster tall tower sites in

561     Switzerland described below.

562     3.3.1. Tests at the High Altitude Research station Jungfraujoch

563     The High Alpine research station Jungfraujoch is located on the northern ridge of the

564     Swiss Alps (46° 33′ N, 7° 59′ E) at an elevation of 3580 m a.s.l. It is one of the global

565     atmospheric watch (GAW) stations well-equipped for measurements of numerous species and

566     aerosols. The site is above the planetary boundary layer most of the time due to its high

567     elevation (Henne et al., 2010; Zellweger et al., 2003). However, thermally uplifted air from

568     the surrounding valleys during hot summer days or polluted air from the heavily industrialized

569     northern Italy may reach at this site (Zellweger et al., 2003). The Division of Climate and

570     Environmental Physics at the University of Bern has been monitoring $CO_2$ and $O_2$ mixing

571 ratios at this site based on weekly flask sampling and continuous measurements since 2000

572 and 2004, respectively (Schibig et al., 2015). The $CO_2$ mixing ratio is measured using a

573 commercial NDIR analyzer (S710 UNOR, SICK MAIHAK) while $O_2$ is measured using the

574 Paramagnetic sensor (PM1155 oxygen transducer, Servomex Ltd, UK) and fuel cells (Max-

575 250, Maxtec, USA) installed inside a home-built controlling unit. Similar to the comparison

576 tests at the University of Bern, we have conducted parallel measurements between the CRDS

577 analyzer and the paramagnetic cell at this high altitude site during 03 – 14 February 2017. The

578 measurement of ambient air at the Jungfraujoch system is composed of sequential switching

579 between low span (LS) and high span (HS) calibration gases followed by a target gas (T)

580 measurement (once a day) to evaluate the overall system performance and finally a working

581 gas (WG) measurement before switching back to ambient air.

582   Figure 16 (top panel) shows the calibrated 1-minute averaged $O_2$ mixing ratios

583 measured at this high altitude site in comparison with the Paramagnetic oxygen analyzer

584 already available at the site. Despite the strong variability observed during the measurement

585 period of 10-days by both analyzers, a very good agreement was observed between them.

586   Figure 16 (bottom panel) shows the absolute difference of 1-minute averages in

587 atmospheric $O_2$ measured at Jungfraujoch between the two analyzers which are mostly within

588 ±5 ppm range (but sometimes going as high as ±10 ppm) without an offset. However, for

589 generally reported 10-minutes, half-hourly or hourly means these values correspond to < 1.5

590 ppm, < 1 ppm and < 0.65 ppm.

591  3.3.2. Tests at the Beromünster tall tower site

592   The Beromünster tower is located near the southern border of the Swiss Plateau, the

593 comparatively flat part of Switzerland between the Alps in the south and the Jura mountains

594 in the northwest (47° 11′ 23″ N, 8° 10' 32″ E, 797 m a.s.l.), which is characterized by intense

595  agriculture and rather high population density. A detailed description of the tower

596  measurement system as well as a characterization of the site with respect to local

597  meteorological conditions, seasonal and diurnal variations of greenhouse gases, and regional

598  representativeness can be obtained from previous publications (Berhanu et al., 2016; Berhanu

599  et al., 2017; Oney et al., 2015; Satar et al., 2016). The tower is 217.5 m tall with access to five

600  sampling heights (12.5 m, 44.6 m, 71.5 m, 131.6 m, 212.5 m) for measuring CO, $CO_2$, $CH_4$

601  and $H_2O$ using Cavity Ring Down Spectroscopy (Picarro Inc., G-2401). By sequentially

602  switching from the highest to the lowest level, mixing ratios of these trace gases were

603  recorded continuously for three minutes per height, but only the last 60 seconds were retained

604  for data analysis. The calibration procedure for ambient air includes measurements of

605  reference gases with high and low mixing ratios traceable to international standards (WMO-

606  X2007 for $CO_2$ and WMO-X2004 for CO and $CH_4$), as well as target gas and more frequent

607  working gas determinations to ensure the quality of the measurement system. From two years

608  of data a long-term reproducibility of 2.79 ppb, 0.05 ppm, and 0.29 ppb for CO, $CO_2$ and

609  $CH_4$, respectively was determined for this system (Berhanu et al., 2016).

610  Between 15.02.2017 and 02.03.2017, we have connected the new CRDS oxygen

611  analyzer in series with the $CO_2$ analyzer (Picarro G-2401) and measured the $O_2$ mixing ratios

612  at the corresponding heights. Similar to the $CO_2$ measurements, $O_2$ was also measured for

613  three minutes at each height. During this period, we have evaluated the two features (isotopic

614  mode and concentration mode) of the CRDS analyzer. In the isotopic mode, the CRDS

615  measures the $\delta^{18}O$ values as well as the $O_2$ concentration while in concentration mode only

616  the latter was measured.

617  During the tests conducted at this tower site, we first evaluated the two operational

618  modes (concentration vs isotopic modes) of the CRDS analyzer. Ambient air measurements

on isotopic mode over a 4-days period showed a strong variability in the measured oxygen

mixing ratios and it was not possible to distinguish the variability in the $O_2$ mixing ratios

among the five height levels. The calculated 1-minute standard error for ambient air

measurements was as high as 10 ppm while a standard error of less than 1 ppm was

determined from similar measurements in the concentration mode. Additionally, comparing

the $O_2$ values between the two modes, frequent short time variation in ambient air $O_2$ (~ 200

ppm) was observed in the isotope mode measurements while the variation in the concentration

mode is significantly smaller (~ 30 ppm). This precision degradation is due to the weaker $^{16}O$

oxygen line used for the isotopic mode, and the fact that far more ring-downs are collected on

the rare isotopologue in isotopic mode Hence, we have conducted the remaining test

measurements in concentration mode.

As this tower has five sampling height levels, we first followed three minutes of

switching per inlet level, which enables four measurements per hour at a given level.

However, we noticed hardly any difference among the different levels due to strong short

term variability in $O_2$ mixing ratios between the consecutive heights. Hence, we switched to a

longer sampling period of six-minutes per height. Figure 17 shows the diurnal $CO_2$ and $O_2$

variations at the lowest (12 m) and highest (212.5 m) sampling heights of the tower. These

two heights were selected simply to better illustrate the difference in the mixing ratios. The

$CO_2$ mixing ratios on the top panel show higher values at the 12 m inlet than the highest level

most of the day due to its closeness to sources except during the afternoon (11:00 - 17:00

UTC) when both levels show similar but decreasing $CO_2$ mixing ratios. This is due to

presence of a well-mixed planetary boundary layer (PBL) (Satar et al., 2016). The lag in $CO_2$

peak between the two height levels by about two hours indicates the duration for uniform

vertical mixing along the tower during winter 2017. The opposite variability patterns are also

643  clearly visible in the $O_2$ mixing ratios shown in the lower panel with a clear distinction

644  between the two height levels during early in the morning and in the evening while similar $O_2$

645  values were observed in the afternoon. These opposing profiles are expected as $CO_2$ and $O_2$

646  are linearly coupled with a mean oxidation ratio of -1.1 ± 0.05 (Severinghaus, 1995) for land-

647  biospheric processes (photosynthesis and respiration) and -1.44 ± 0.03 for fossil fuel burning

648  (Keeling, 1988b).

649  Table 2 shows the oxidation ratios derived as the slopes of the linear regression

650  between $CO_2$ and $O_2$ mixing ratios at the different height levels measured on 25 February

651  2017. Accordingly, height dependent slopes were observed with a slope of -0.98 ± 0.06 at the

652  lowest level, close to the biological processes induced slope but slightly lower than its mean

653  value. For the highest level, we calculated a slope of -1.60 ± 0.07 a value close to fossil fuel

654  combustion oxidation ratio. Note that depending on fossil fuel type the oxidation ratio can

655  range between -1.17 and -1.95 for coal and natural gas, respectively (Keeling, 1988b). While

656  the slopes derived for the two other levels (44.6 m and 131.6 m) show similar values between

657  the highest and lowest height levels, possibly from mixed sources, the middle level showed a

658  slightly higher slope than these two levels but still in the large range between the lowest and

659  highest inlet heights.

660  3.4. Evaluation of the $\delta^{18}O$ measurements

661  To further evaluate the analyzer's performance in measuring stable oxygen isotopes,

662  we conducted ambient air isotopic composition measurements as well as analyzed a standard

663  gas without $CO_2$ which has a known $\delta^{18}O$ value. The choice of this $CO_2$-free air standard gas

664  is twofold: one it has a known $\delta^{18}O$ value and second as it has no interference from possible

665  $CO_2$ absorption band overlap. For this test three 0.5 L glass flasks were preconditioned and

666  filled with this standard gas to ambient pressure. These flasks were attached before or after

the water trap (Fig. 11) and measured similar to ambient air measurements. These measurements were then compared with $\delta(^{34}O/^{32}O)$ values obtained by parallel measurements using our IRMS.

Figure 18 shows the $\delta^{18}O$ values of ambient air from the roof top with three consecutive measurements of glass flasks filled with $CO_2$-free air in-between followed by a fourth flask filled with breath air. An excellent agreement was observed for measurements from both instruments for the three flasks filled with a standard gas. However, the fourth flask with breath air showed a signal opposite to the measurements by the IRMS. As breath air contains large amount of water and $CO_2$ in addition to $O_2$, which can possibly interfere with the CRDS analyzer measurements, we have removed $H_2O$ and $CO_2$ by using a cryogenic trap (-130 °C) and in an additional experiment using Schütze reagent to remove both CO and $CO_2$. However, we have not observed any improvement towards an agreement with the IRMS measurements. Therefore, any other gas component in the breath air must be relevant for the interference. Based on the absorption lines in the spectral range of the instrument (7878 cm$^{-1}$) retrieved from HITRAN database, we expect interference either from carbon monoxide (now excluded by the tests) or methane or VOCs including acetone, ethanol, methanol or isoprenes, all of which have been measured in breath air (Gao et al., 2017; Gottlieb et al., 2017; Mckay et al., 1985; Ryter and Choi, 2013; Wolf et al., 2017). Further investigations have to shed light on these interferences in order to take corresponding action to surpass these shortcomings in the isotope analysis based on cavity ring-down spectroscopy.

**4. Conclusions**

We have thoroughly evaluated the performance of a new CRDS analyzer which measures $O_2$ mixing ratios and isotopic composition combining laboratory and field tests. Even if a drift in the analyzer was observed at the beginning of this study, which can be easily

691  corrected by calibration, the recent analyzers built by the manufacturer did not show such

692  instrumental drift. However, prior tests are recommended to see the analyzer's stability.

693      The T-split tests for the current measurement setup based on the measurements of two

694  standard gases showed a difference within the measurement uncertainty. However, this effect

695  may become significant while applying larger splitting ratios and we recommend conducting

696  further experiments to accurately quantify this influence for larger splitting ratios.

697      We have observed a strong influence of dilution in the measured $O_2$ values during the

698  presence of high $CO_2$ mixing ratios. Even if such an influence may not be critical for the

699  present study, such an effect might be significant in other studies where higher $CO_2$ mixing

700  ratios might be present and we recommend following a correction strategy based on parallel

701  $CO_2$ measurements. This also applies for more accurate analysis.

702      The water correction applied by the instrument's in-built function seems to sufficiently

703  correct for the water vapor influence. However, a larger variability of the difference was

704  observed between the CRDS analyzer and the Paramagnetic cell when dried samples were

705  used in both systems. This can possibly be due to an overcorrection by the water correction

706  function of the CRDS analyzer when dried samples were used. This is particularly true for the

707  very low water vapor range (< 100 ppm). We believe that it is important to further investigate

708  this issue and identify an improved water correction strategy.

709      Based on the analysis of $O_2$ mixing ratios in the concentration and isotopic modes, we

710  have observed a significant decrease in precision (about ten-fold) in the latter measurement

711  mode. The measured $\delta^{18}O$ values for the standard air by the CRDS analyzer are in excellent

712  agreement with the IRMS values. However, such measurements for a breath air showed a

713  contrasting signal, possibly due to interference from other gases such as $CH_4$. Hence, we

714  recommend further investigation on such possible contaminants and how to possibly remove

715  them while conducting ambient air measurements. However, we believe that this analyzer can

716  be used for tracer experiments where artificially enriched isotopes are used to study biological

717  processes such as photosynthesis in plants using isotopically labelled $CO_2$ and $H_2O$.

718  **Acknowledgement**

719  We would like to thank ICOS-RI and the Swiss National Science Foundation (SNF) for

720  funding ICOS-CH (20FI21_148994, 20FI21_148992). We are also grateful to the

721  International Foundation High Alpine Research Stations Jungfraujoch and Gornergrat. The

722  measurement system at the Beromünster tower was built and maintained by the CarboCount-

723  CH (CRSII2_136273) and IsoCEP (200020_172550) projects both funded by SNF.

724

725

726

727

728

729

730

731

732

733  List of Tables

734  Table 1. Assigned mixing ratios of standard gases used in this study and their corresponding

735  values measured by the NDIR, CRDS and IRMS at the University of Bern. [1]The assigned

736  values are based on measurements from different institutions (University of Bern (UB),

737  Scripps or NOAA, see column cylinder name). [2]Measurements are on the Bern scale for $CO_2$

738  and $O_2$. The Bern scale is shifted by +550 per meg. [3]Values on the Scripps scale.

739

| Cylinder name | Assigned $CO_2$ (ppm)[1] | Assigned $O_2$ (per meg)[1] | $CO_2$-IRMS (ppm)[2] | $CO_2$-NDIR (ppm)[2] | $O_2$-IRMS (per meg)[2] | $O_2$-Paramagnetic (per meg)[2] | $O_2$-CRDS (per meg)[2] |
|---|---|---|---|---|---|---|---|
| ST-1 LUX3576-UB | 427.47 | -1026 | 427.47 | 427.59 | -1026 | -1070 | -1057 |
| ST-2 LK922131-UB | 368.09 | 599 | 368.09 | 367.82 | 599 | 560 | 590 |
| ST-3 CA07045-Scripps | 382.303 | -271.6 | 382.50 | 381.99 | 278 (-272.2)[3] | 302 | 281 |
| ST-4 CA07043-Scripps | 390.528 | -476.4 | 390.69 | 390.15 | 71 (-479.5)[3] | 66 | 63 |
| ST-5 CA07047-Scripps | 374.480 | -807.7 | 374.70 | 374.17 | -253 (-803.3)[3] | -212 | -233 |
| ST-6 CA04556-NOAA | 192.44 | -3410 | 191.21 | 191.64 | -3410 | -2905 | -3013 |
| ST-7 CA06943-NOAA | 2699.45 | - | | 2612.80 | - | -2691 | -3369 |
| ST-8 LK76852-UB | 411.49 | 37794 | 411.49 | 406.25 | 37794 | 34513 | 36017 |

740

741

742    Table 2. The $CO_2$ and $O_2$ correlation coefficients at the different height levels derived using

743    the least square fit and the correlation coefficients ($r^2$). Uncertainties are calculated as

744    standard error of the slope.

| Height | Oxidation Ratios ($O_2$:$CO_2$) |
|--------|--------------------------------|
| 12.5 m | -0.98 ± 0.06 (0.48) |
| 44.6 m | -1.29 ± 0.07 (0.50) |
| 71.5 m | -1.49 ± 0.08 (0.47) |
| 131.6 m | -1.23 ± 0.05 (0.55) |
| 212.5 m | -1.60 ± 0.07 (0.61) |

745

746

747

748

749

750

751

752

753    List of Figures

754
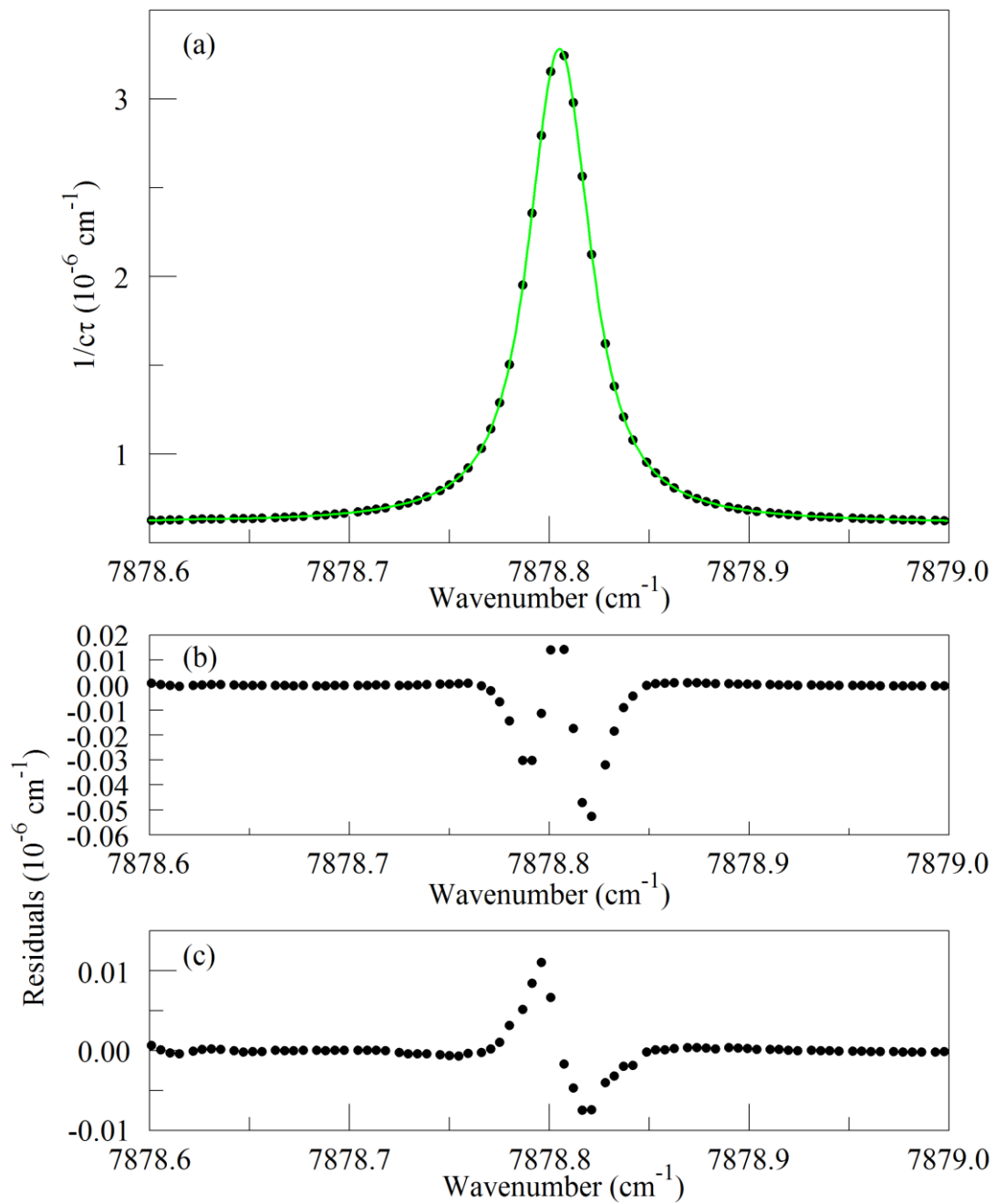
Figure 1. The top panel (a) shows the raw data (points) and the best-fit Galatry function (solid

line). Residuals of the Voigt fit are shown in panel (b) and residuals of the Galatry fit are

shown in panel (c).

758

759
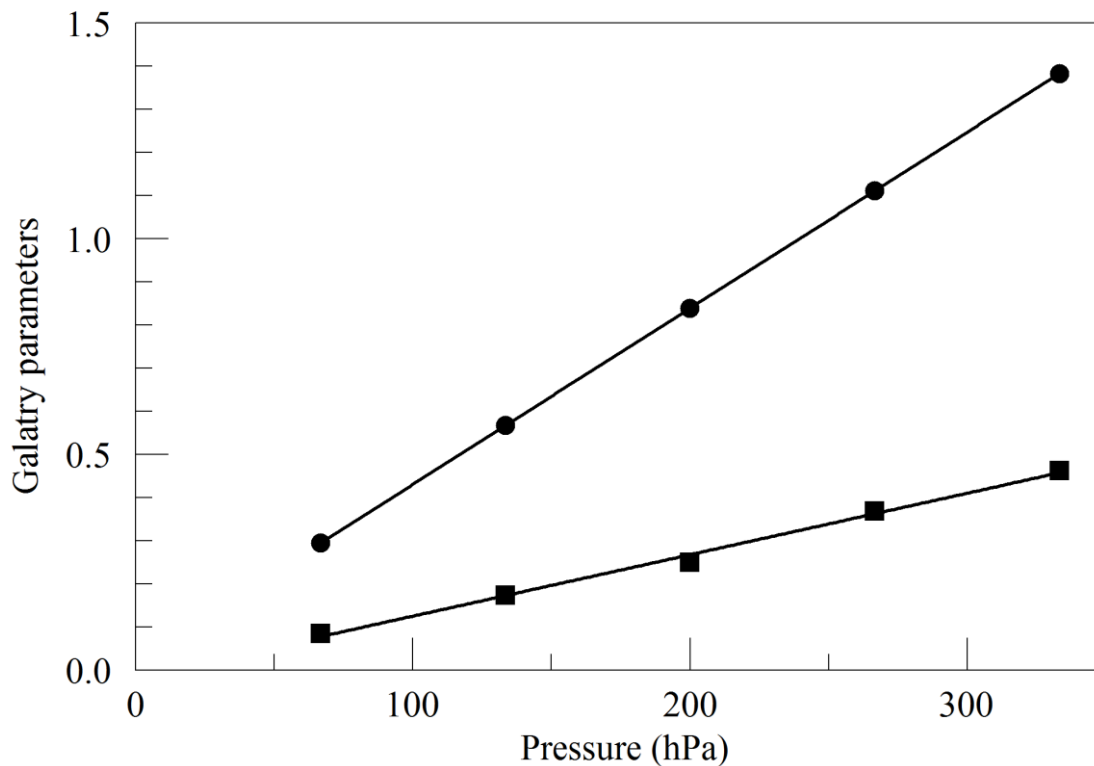
760

761    Figure 2.  Best-fit values for the Galatry parameters of the Q13Q13 line of $O_2$, as a function of

762    pressure. The line broadening parameter y is represented by circles and the line narrowing

763    parameter z by squares. The solid lines are linear fits to the measurements. The best-fit offset

764    and slope are 0.0227 and 0.004082 $hPa^{-1}$ for y, and -0.0169 and 0.001424 $hPa^{-1}$ for z.
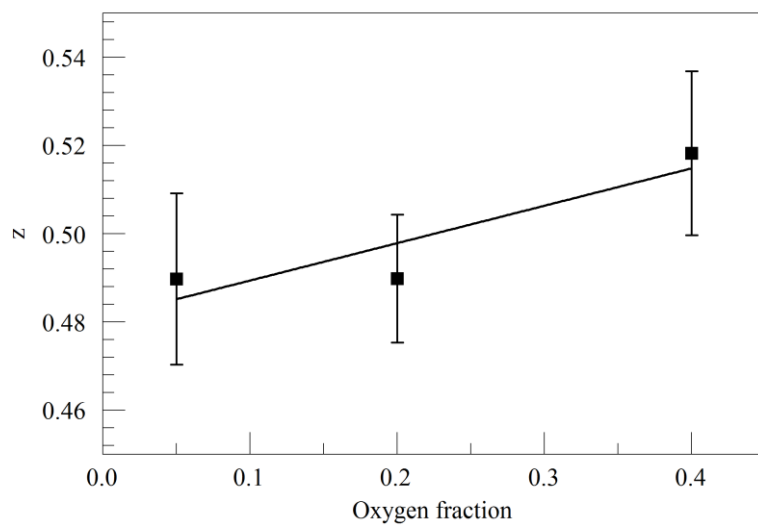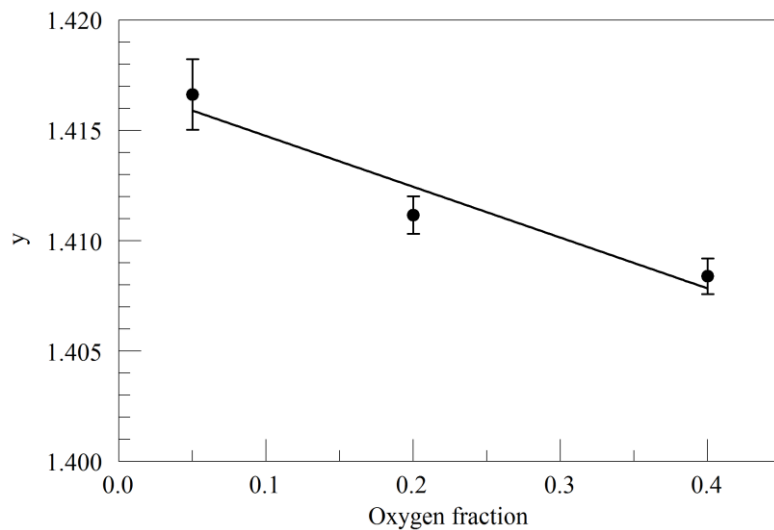
765

766    Figure 3.  Galatry parameters of the Q13Q13 line of $O_2$ at 340 hPa and 45° C as a function of

767    $O_2$ mole fraction in binary $O_2$ - $N_2$ mixtures. The linear fits to the data are y = 1.417 – 0.023 x

768    $f_{O2}$ and z = 0.481 + 0.085 x $f_{O2}$.
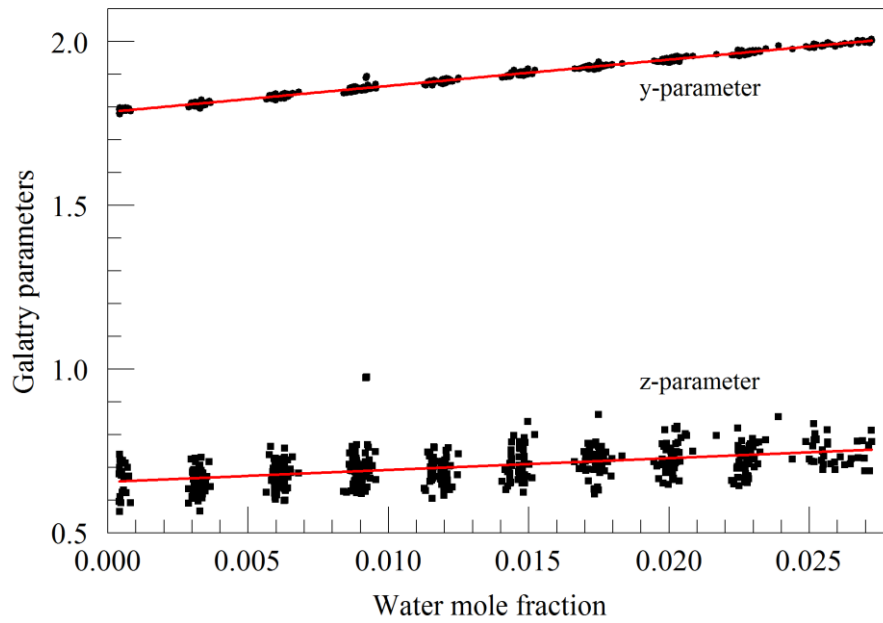
769

770    Figure 4. Galatry parameters of the 7816.75210 cm$^{-1}$ water line in air at 340 hPa and 45° C as

771    a function of water mole fraction. Black points are from measurements and red lines are

772    linear fits: $y = 1.7846 + 8.01 \times f_{H2O}$ and $z = 0.656 + 3.60 \times f_{H2O}$.

773

774

775
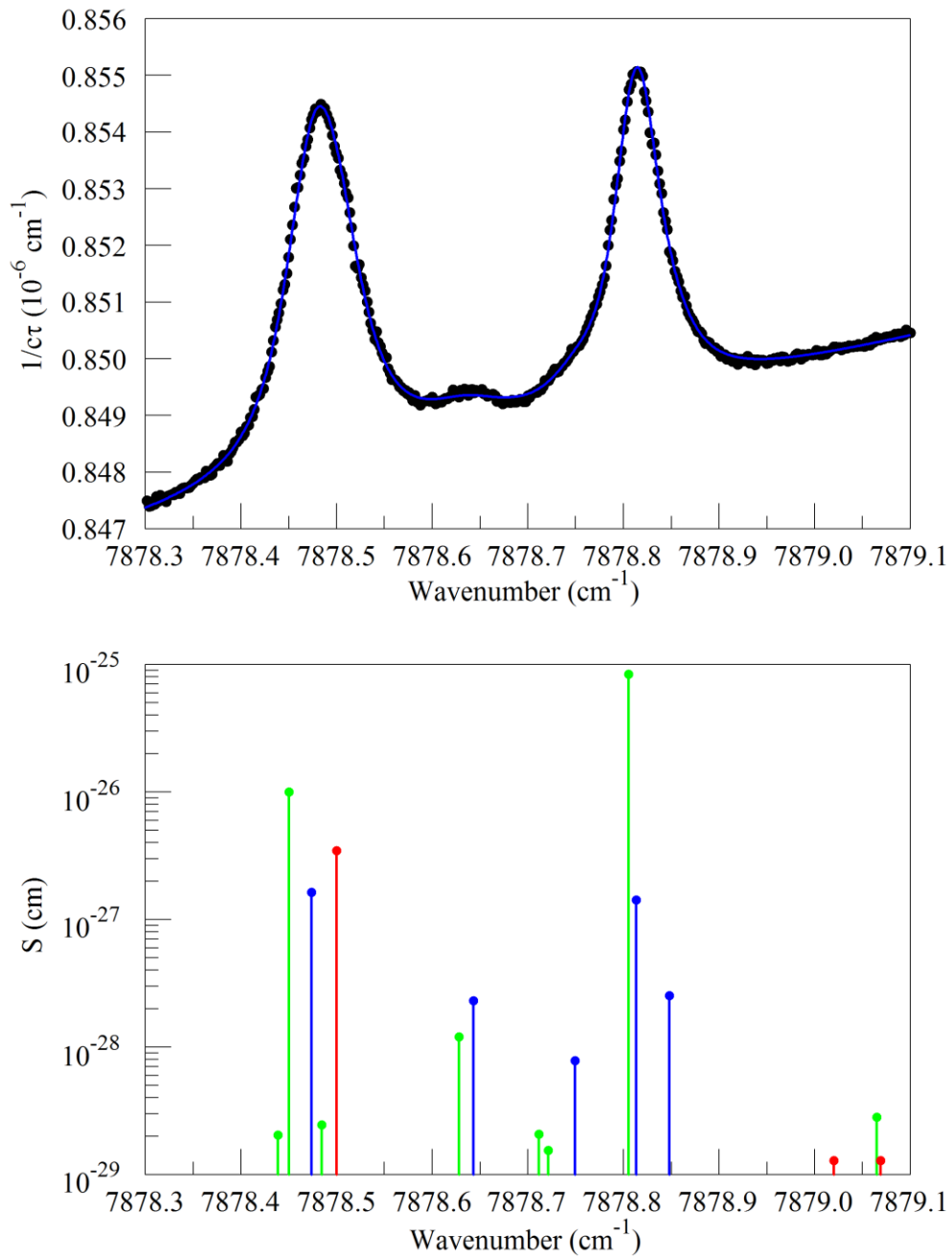
Figure 5. Upper panel: spectrum of water in nitrogen (points) and fit to Voigt model (blue curve). Lower panel: Oxygen (green), normal water (blue), and deuterated water (red) lines in the 2016 Hitran data base.
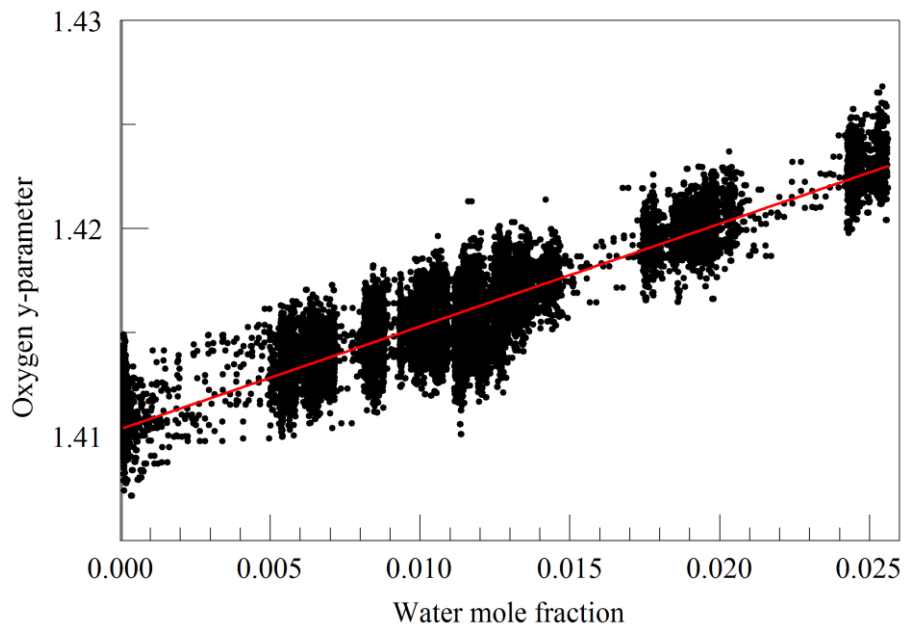
782

783 Figure 6. Galatry collisional broadening parameter of the oxygen Q13Q13 line at 340 hPa

784 and 45° C versus water mole fraction. Black points are from measurements and the red line is

785 a linear fit: $y = 1.4109 + 0.467\ f_{H2O}$.

786

787

788
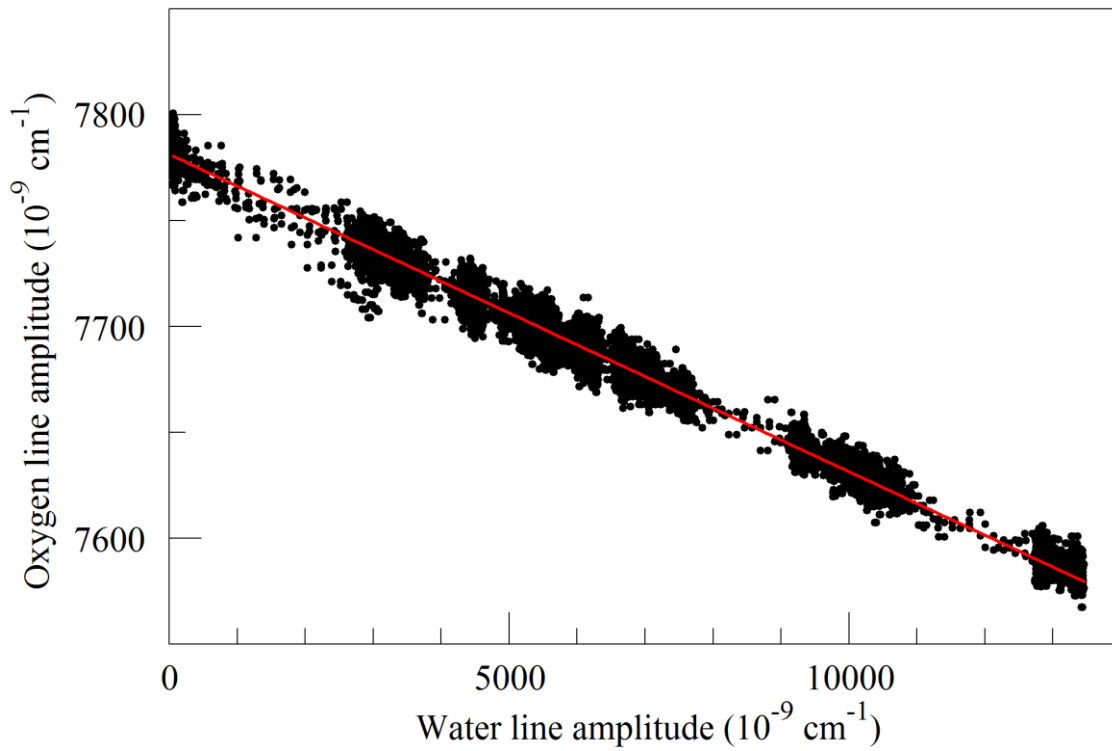
789

790      Figure 7. Measured absorption line amplitudes for oxygen and water vapor for water vapor

791      mixing ratios ranging from nearly 0 to 0.025. Black points are from measurements and the

792      red line is a linear fit: with intercept $7.78001 \times 10^{-6}$ cm$^{-1}$ and slope -0.014807.

793

794

795

796

797

798

799
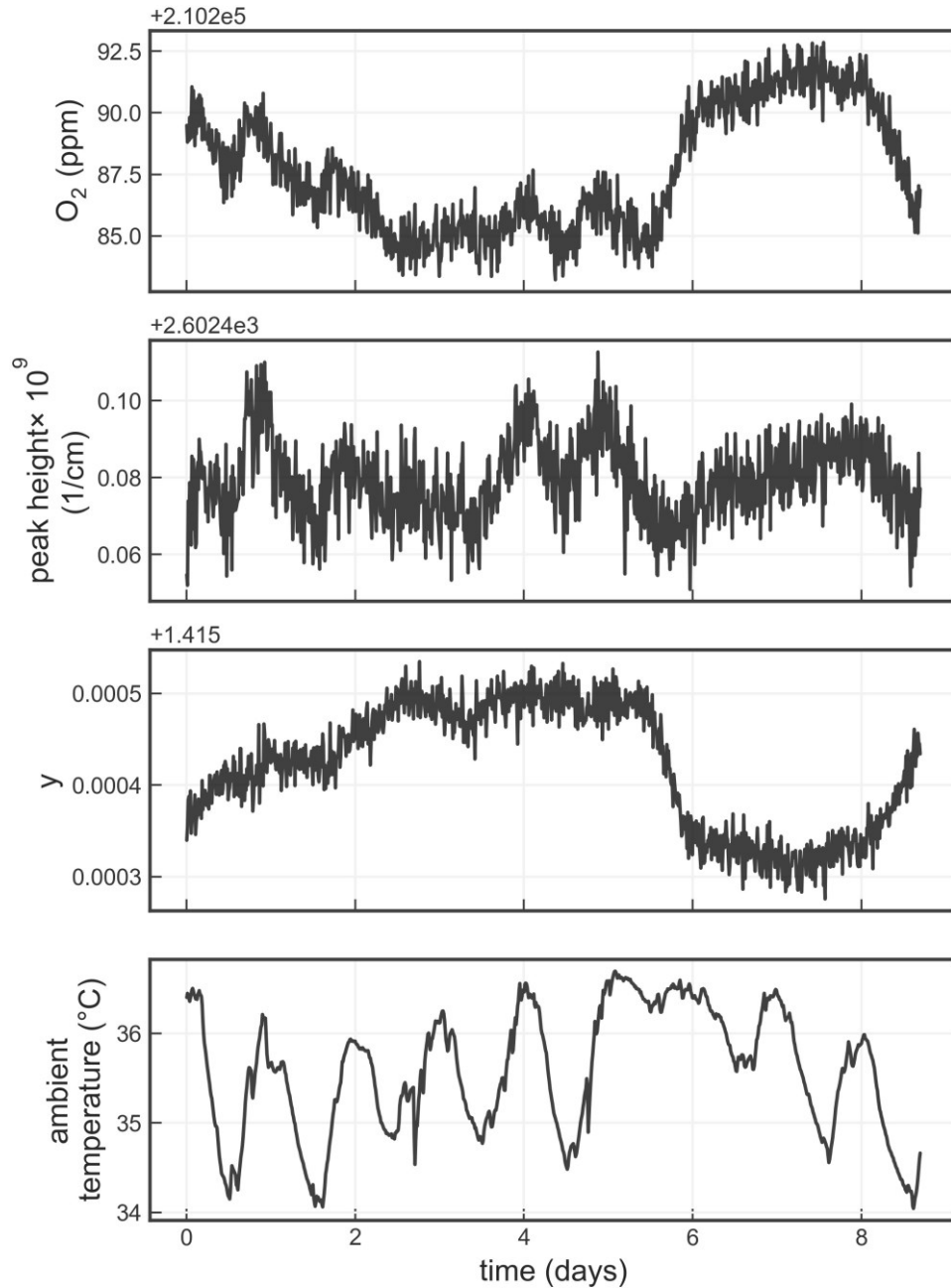
Figure 8. Time series from a measurement of a single tank over about a week. The four panels
show the water-corrected oxygen concentration, the absorption peak loss minus the baseline
loss, the measured Lorentzian broadening factor, and the ambient temperature (measured in
the instrument housing), respectively. A windowed average of 300 seconds was applied to all
four data sets.
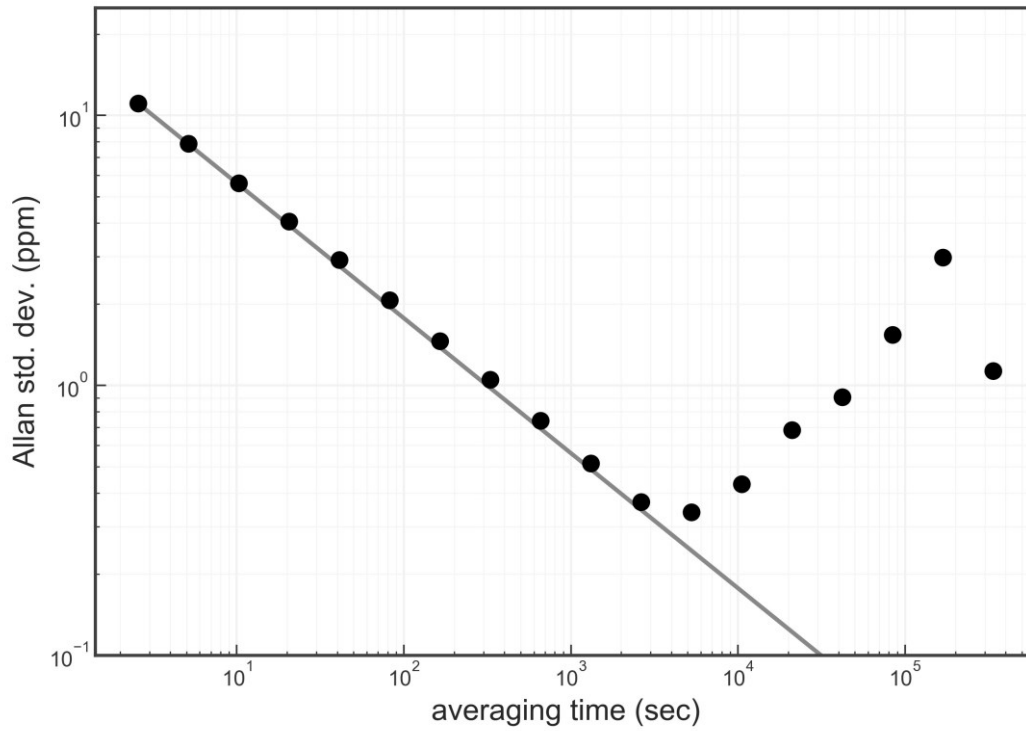
805

806    Figure 9. Precision of $O_2$ mole fraction measured from a tank of synthetic air.  Filled circles

807    are measurements and the line shows the ideal $\tau^{-1/2}$ dependence.

808

809

810

811

812

813
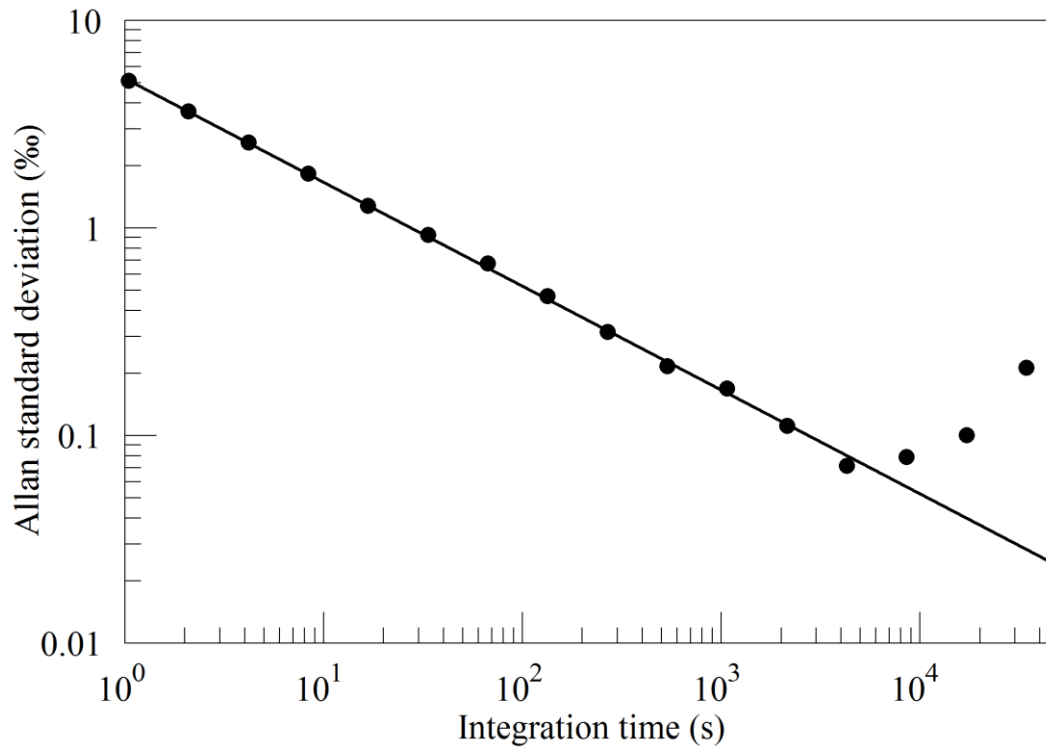
Figure 10. Precision of $\delta(^{18}O)$ measured from a tank of synthetic air. Filled circles are

815 measurements and the line shows the ideal $\tau^{-1/2}$ dependence.

816

817

818

819

820

821

822

823
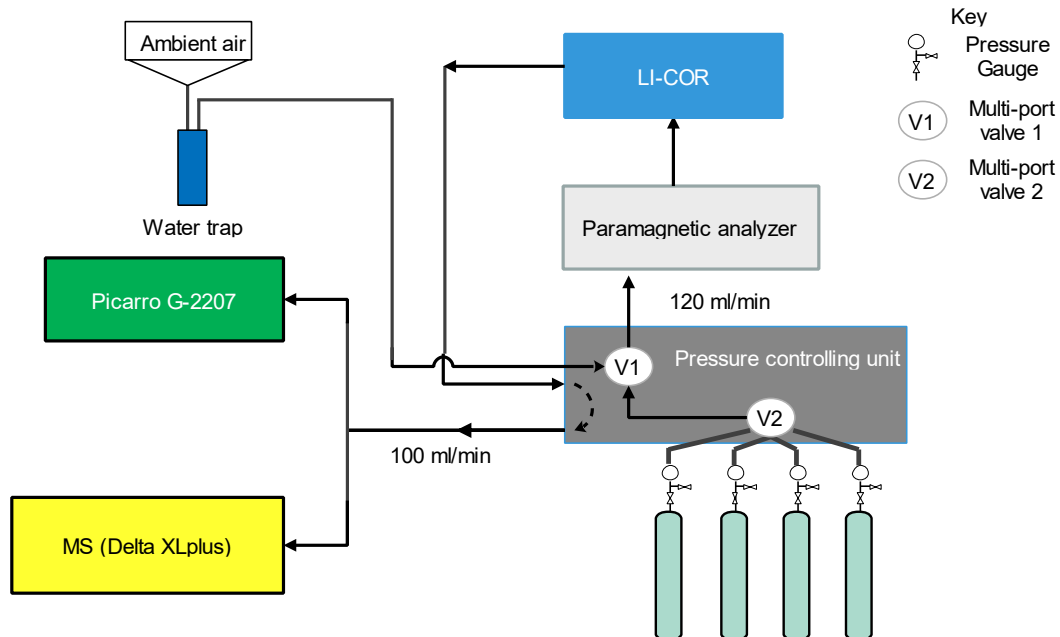
824

825    Figure 11. Schematics of the measurement system used to compare the Picarro analyzer with

826    the Mass Spectrometer at Bern.

827

828

829

830

831

832

833

834

835
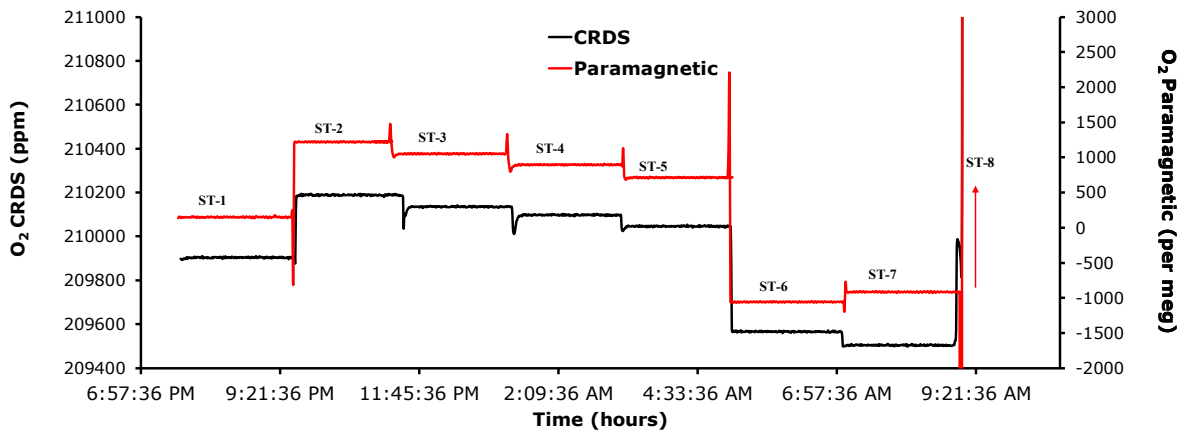
836

837 Figure 12. Comparison of oxygen mixing ratios for the seven standard gases measured using

838 the CRDS analyzer (black) and the Paramagnetic sensors (red).

839

840

841

842

843

844

845

846

847

848

849

850

851

852

853

854
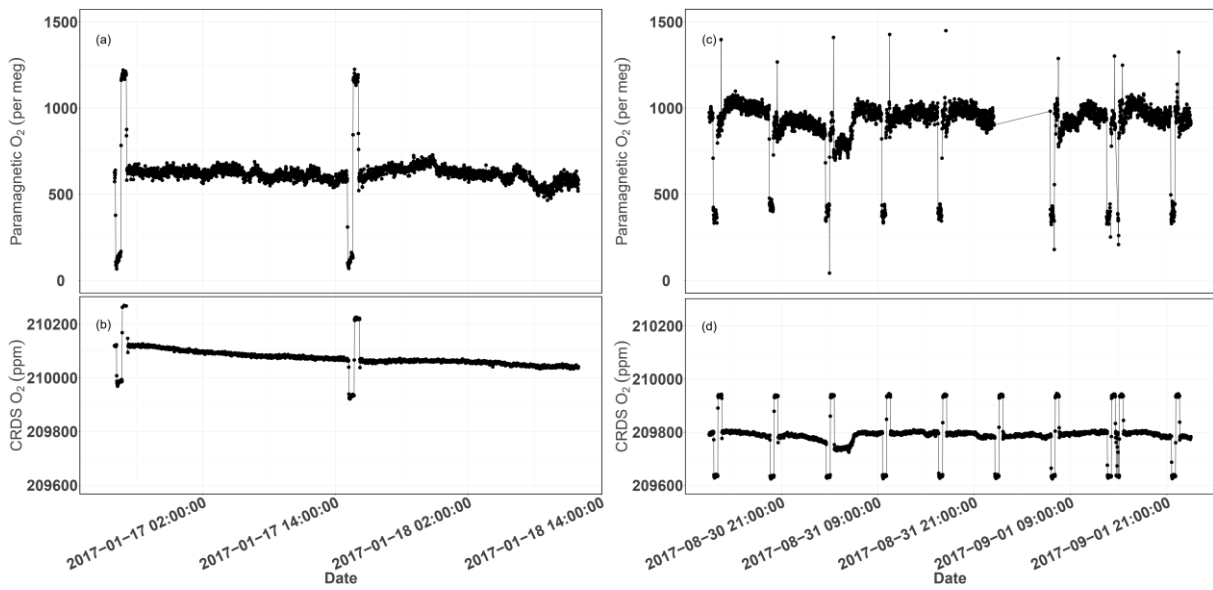
855

856    Figure 13. Parallel ambient air measurements by the Paramagnetic and CRDS analyzers at the

857    beginning of the testing period (Panels a & b, January 2017) and the second phase of testing

858    (Panels c & d, September 2017). The spikes are measurements from the two standard gases

859    bracketing the ambient air values.

860

861

862

863

864

865

866

867

868

869

870

871
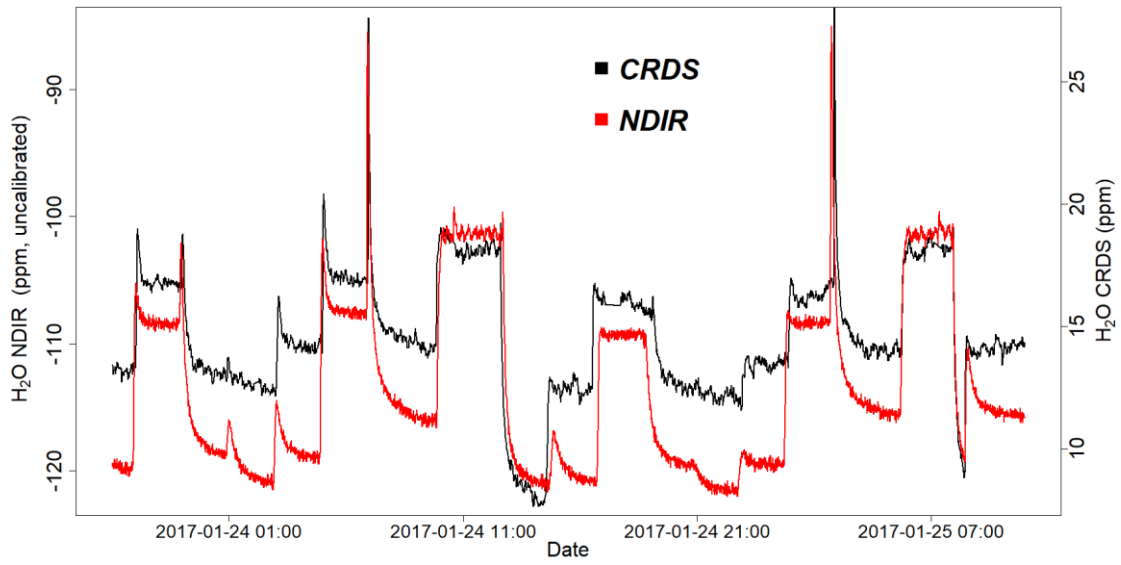
872

873    Figure 14. Parallel water vapor measurements for a dried ambient air by both the NDIR and

874    CRDS analyzers. Note that the water values from the NDIR analyzer are not calibrated.

875

876

877

878

879

880

881

882

883

884

885

886

887

888

889
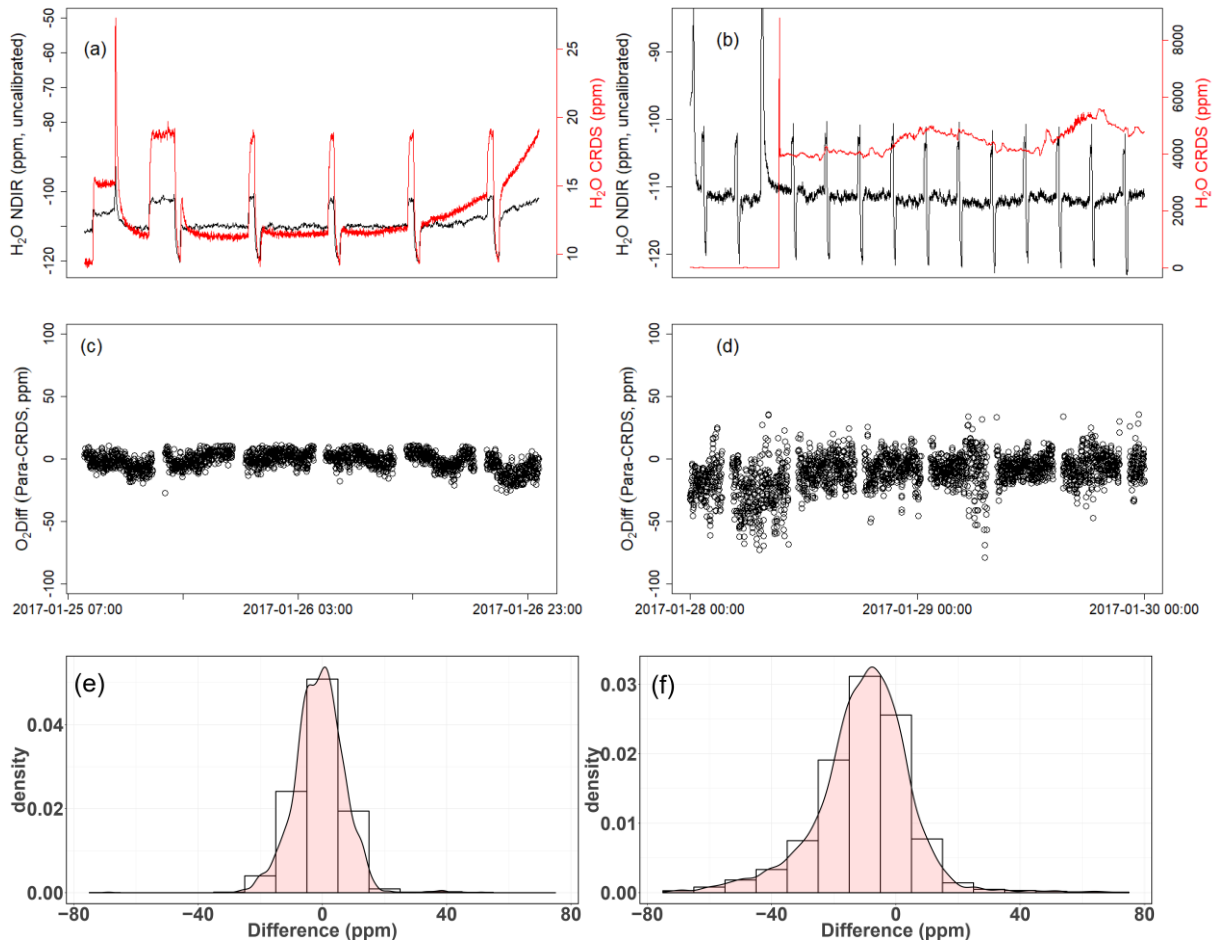
Figure 15. Results of water correction tests. Water measurements of the NDIR (left scale) for

dry conditions (a,b) and the CRDS analyzer (right scale) for dry (a) and wet (b) conditions.

The difference in oxygen measurements between the Paramagnetic and the CRDS instrument

using the built-in water correction for the CRDS values under dry (c) and wet (d) conditions.

Panels (e) and (f) show the population density functions.

895

896

897

898

899

900

901
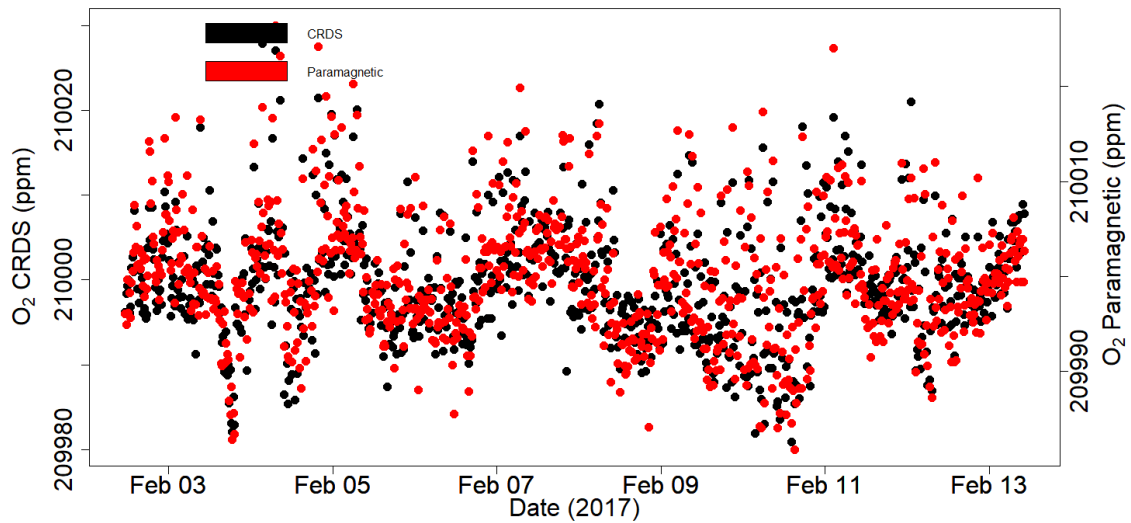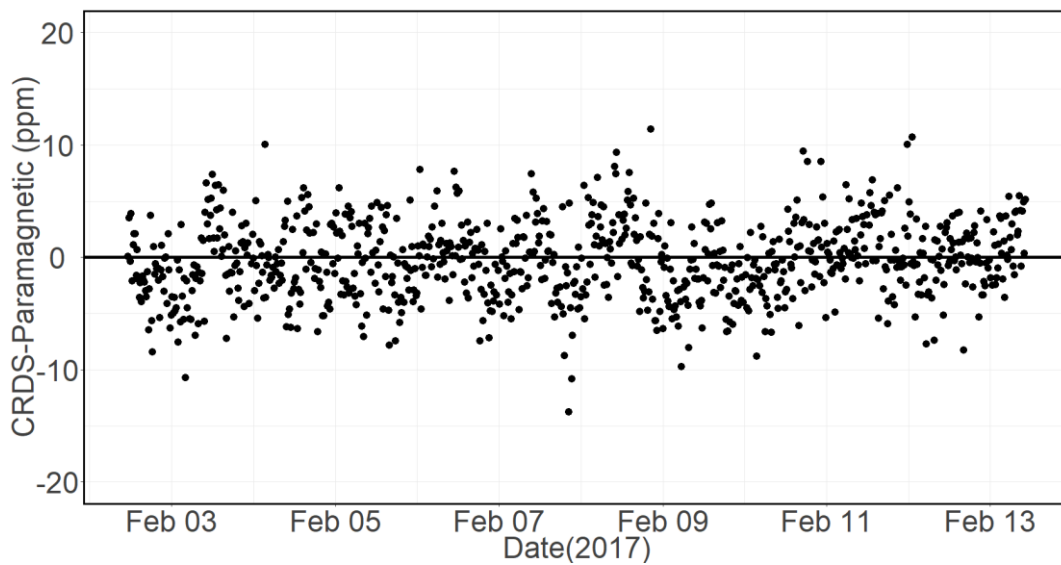
Figure 16. Calibrated ambient air oxygen measurements (1-minute average) at the

Jungfraujoch site using the CRDS and Paramagnetic analyzers both in ppm units (a) and the

absolute difference between the two measurements in ppm (b) by matching time stamps

905

906

907

908

909
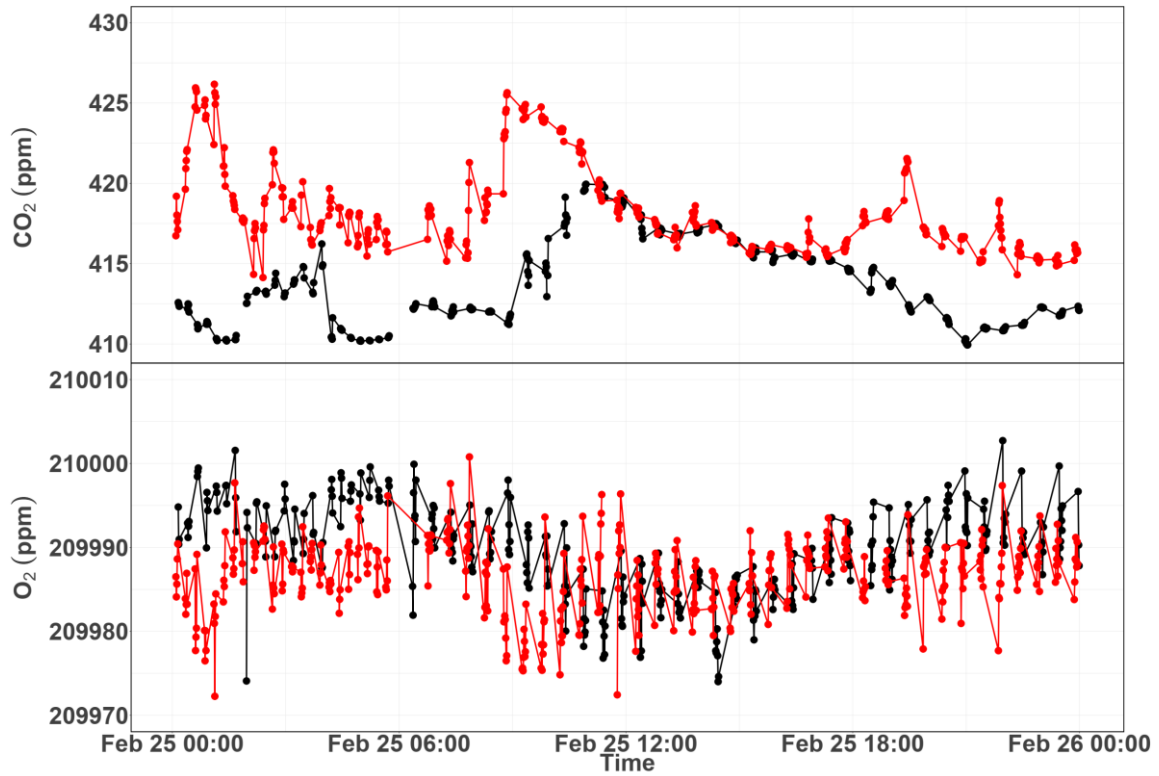
910

911    Figure 17. Diurnal variations of $CO_2$ (top) and $O_2$ (bottom) measurements from the 12 m (red)

912    and the 212.5 m (black) height levels at Beromünster tower.

913

914

915

916

917

918

919

920

921

922
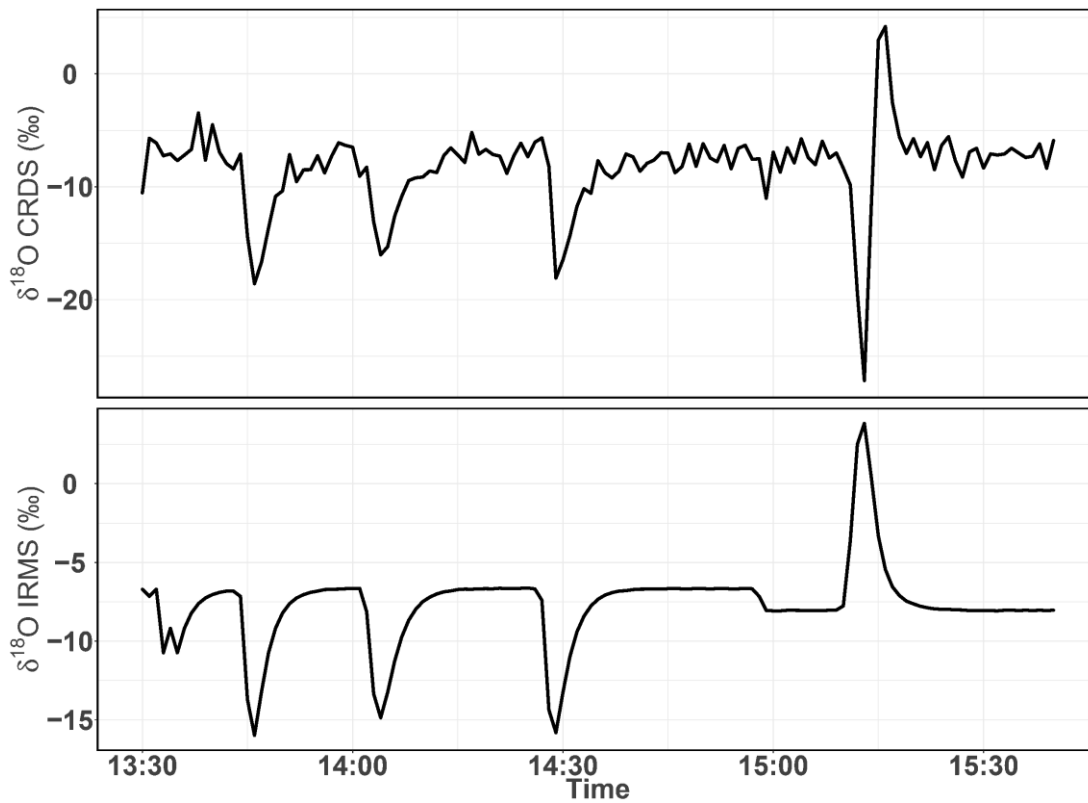
923

924    Figure 18. Consecutive $\delta^{18}O$ measurements of a standard gas ($CO_2$-free air) filled into three

925    flasks followed by measurement of breath air using the CRDS analyzer (top) and IRMS

926    (bottom). These measurements were carried out in the middle of ambient air measurements.

927

928

929

930

931

932

933

934

935

936

937 **Appendix A.**

938
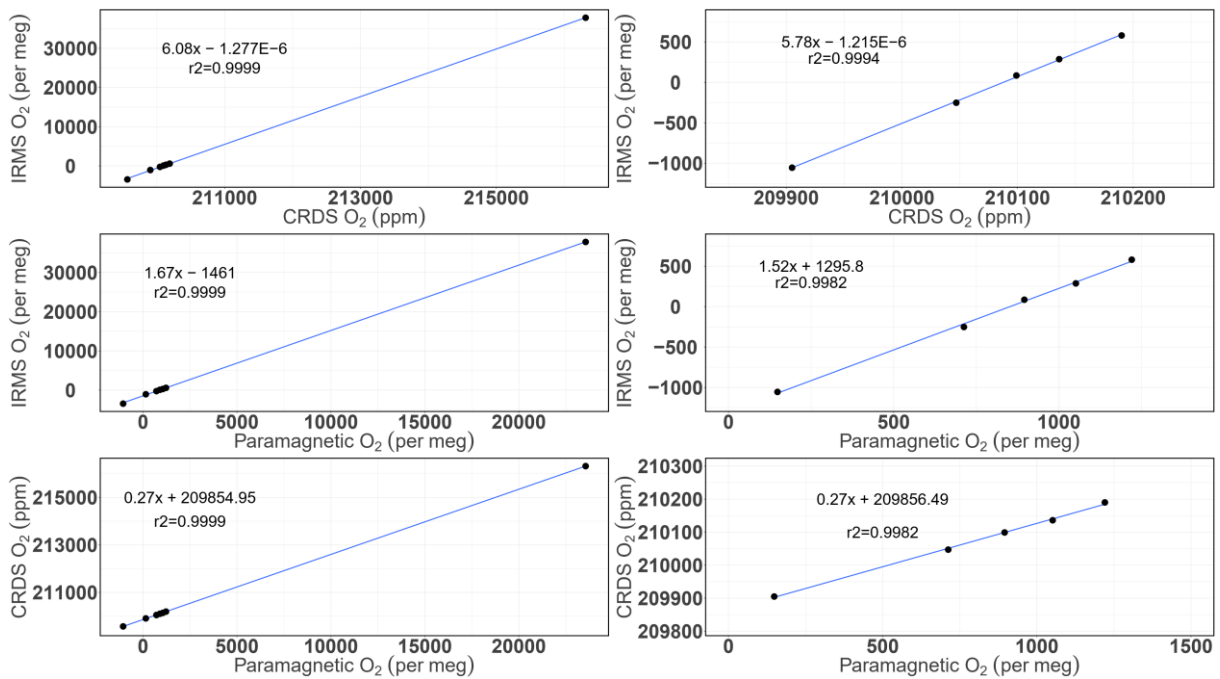
939

940 Figure A.1. Correlations between the $O_2$ mixing ratios measured by the CRDS and

941 Paramagnetic analyzers with the mass spectrometric measurements (uncalibrated values). The

942 left panels are for all the cylinders measured (standards 1 to 8) while the right ones are after

943 selecting standards 1-5.

944

945

946

947

948

949

950

951

952    **References**

953    Battle, M., Bender, M. L., Tans, P. P., White, J. W. C., Ellis, J. T., Conway, T., and Francey, R. J.: Global

954    carbon sinks and their variability inferred from atmospheric O-2 and delta C-13, Science, 287, 2467-

955    2470, 2000.

956    Bender, M. L., Tans, P. P., Ellis, J. T., Orchardo, J., and Habfast, K.: A High-Precision Isotope Ratio

957    Mass-Spectrometry Method for Measuring the O-2 N-2 Ratio of Air, Geochim Cosmochim Ac, 58,

958    4751-4758, 1994.

959    Berhanu, T. A., Satar, E., Schanda, R., Nyfeler, P., Moret, H., Brunner, D., Oney, B., and Leuenberger,

960    M.: Measurements of greenhouse gases at Beromünster tall tower station in Switzerland, Atmos.

961    Meas. Tech. , 9, 2016.

962    Berhanu, T. A., Szidat, S., Brunner, D., Satar, E., Schanda, R., Nyfeler, P., Battaglia, M., Steinbacher,

963    M., Hammer, S., and Leuenberger, M.: Estimation of the fossil-fuel component in atmospheric $CO_2$

964    based on radiocarbon measurements at the Beromünster tall tower, Switzerland, Atmos. Chem.

965    Phys. Discuss., 2017, 1-33, 2017.

966    Crosson, E. R. J. A. P. B.: A cavity ring-down analyzer for measuring atmospheric levels of methane,

967    carbon dioxide, and water vapor, 92, 403-408, 2008.

968    Filges, A., Gerbig, C., Rella, C. W., Hoffnagle, J., Smit, H., Krämer, M., Spelten, N., Rolf, C., Bozóki, Z.,

969    Buchholz, B., and Ebert, V.: Evaluation of the IAGOS-Core GHG Package H2O measurements during

970    the DENCHAR airborne inter-comparison campaign in 2011, Atmos. Meas. Tech., 11, 5279–5297,

971    2018, https://doi.org/10.5194/amt-11-5279-2018. Gao, F., Zhang, X., Zhang, X., Wang, M., and Wang,

972    P.: Virtual electronic nose with diagnosis model for the detection of hydrogen and methane in breath

973    from gastrointestinal bacteria, 28-31 May 2017 2017, 1-3.

974    Gordon, E., Rothman, S., Hill, C., Kochanov, V., Tan, Y., Bernath, P., Birk, M., Boudon, V., Campargue,

975    A., Chance, K., Drouin, J., Flaud, J., Gamache, R. R., Hodges, J., Jacquemart, D., Perevalov, I., Perrin, A.,

976    Shine, P., Smith, M., Tennyson, J., Toon, G., Tran, H., Tyuterev, G., Barbe, A., Császár, G., Devi, M.,

977    Furtenbacher, T., Harrison, J., Hartmann, J., Jolly, A., Johnson, J., Karman, T., Kleiner, I., Kyuberis, A.

978    A., Loos, J., Lyulin, M., Massie, S., Mikhailenko, S., Moazzen-Ahmadi, N., Muller, S., Naumenko, O. V.,

979    Nikitin, A. V., Polyansky, O. L., Rey, M., Rotger, M., Sharpe, S., Sung, K., Starikova, E., Tashkun, S.,

980    Auwera, J., Wagner, G., Wilzewski, J., Wcisło, P., Yu, S., and Zak, E. J.: The HITRAN2016 molecular

981    spectroscopic database, 203, 3 - 69, 2017.

982    Goto, D., Morimoto, S., Ishidoya, S., Aoki, S., and Nakazawa, T.: Terrestrial biospheric and oceanic

983    $CO_2$ uptake estimated from long-term measurements of atmospheric $CO_2$ mole fraction, $\delta13C$ and

984    $\delta(O_2/N_2)$ at Ny-Ålesund, Svalbard, Journal of Geophysical Research: Biogeosciences, doi:

985    10.1002/2017JG003845, 2017. n/a-n/a, 2017.

986    Gottlieb, K., Le, C. X., Wacher, V., Sliman, J., Cruz, C., Porter, T., and Carter, S.: Selection of a cut-off

987    for high- and low-methane producers using a spot-methane breath test: results from a large north

988    American dataset of hydrogen, methane and carbon dioxide measurements in breath, Gastroenterol

989    Rep, 5, 193-199, 2017.

990    Hartmann, J.-M., Boulet, C., and Robert, D.: Collisional Effects on Molecular Spectra, Elsevier Science,

991    2008.

992    Henne, S., Brunner, D., Folini, D., Solberg, S., Klausen, J., and Buchmann, B.: Assessment of

993    parameters describing representativeness of air quality in-situ measurement sites, Atmos. Chem.

994    Phys., 10, 3561-3581, 2010.

995    Hodges, J. T., Layer, H. P., Miller, W. W., and Scace, G. E.: Frequency-stabilized single-mode cavity

996    ring-down apparatus for high-resolution absorption spectroscopy, 75, 849-863, 2004.

997    Keeling, R. F.: Development of an Interferometric Oxygen Analyzer for Precise Measurement of the

998    Atmospheric $O_2$ Mole Fraction, UMI, 1988a.

999    Keeling, R. F.: Measuring correlations between atmospheric oxygen and carbon dioxide mole

1000    fractions: A preliminary study in urban air, J Atmos Chem, 7, 153-176, 1988b.

1001    Keeling, R. F. and Manning, A. C.: 5.15 - Studies of Recent Changes in Atmospheric O2 Content A2 -

1002    Holland, Heinrich D. In: Treatise on Geochemistry (Second Edition), Turekian, K. K. (Ed.), Elsevier,

1003    Oxford, 2014.

1004    Keeling, R. F. and Shertz, S. R.: Seasonal and Interannual Variations in Atmospheric Oxygen and

1005    Implications for the Global Carbon-Cycle, Nature, 358, 723-727, 1992.

1006    Keeling, R. F., Stephens, B. B., Najjar, R. G., Doney, S. C., Archer, D., and Heimann, M.: Seasonal

1007    variations in the atmospheric O-2/N-2 ratio in relation to the kinetics of air-sea gas exchange, Global

1008    Biogeochem Cy, 12, 141-163, 1998.

1009    Lamouroux, J., Sironneau, V., Hodges, J. T., and Hartmann, J. M.: Isolated line shapes of molecular

1010    oxygen: Requantized classical molecular dynamics calculations versus measurements, Physical

1011    Review A, 89, 042504, 2014.

1012    Le Quéré, C., Andrew, R. M., Friedlingstein, P., Sitch, S., Pongratz, J., Manning, A. C., Korsbakken, J. I.,

1013    Peters, G. P., Canadell, J. G., Jackson, R. B., Boden, T. A., Tans, P. P., Andrews, O. D., Arora, V. K.,

1014    Bakker, D. C. E., Barbero, L., Becker, M., Betts, R. A., Bopp, L., Chevallier, F., Chini, L. P., Ciais, P.,

1015    Cosca, C. E., Cross, J., Currie, K., Gasser, T., Harris, I., Hauck, J., Haverd, V., Houghton, R. A., Hunt, C.

1016    W., Hurtt, G., Ilyina, T., Jain, A. K., Kato, E., Kautz, M., Keeling, R. F., Klein Goldewijk, K., Körtzinger, A.,

1017    Landschützer, P., Lefèvre, N., Lenton, A., Lienert, S., Lima, I., Lombardozzi, D., Metzl, N., Millero, F.,

1018    Monteiro, P. M. S., Munro, D. R., Nabel, J. E. M. S., Nakaoka, S. I., Nojiri, Y., Padín, X. A., Peregon, A.,

1019    Pfeil, B., Pierrot, D., Poulter, B., Rehder, G., Reimer, J., Rödenbeck, C., Schwinger, J., Séférian, R.,

1020    Skjelvan, I., Stocker, B. D., Tian, H., Tilbrook, B., van der Laan-Luijkx, I. T., van der Werf, G. R., van

1021    Heuven, S., Viovy, N., Vuichard, N., Walker, A. P., Watson, A. J., Wiltshire, A. J., Zaehle, S., and Zhu,

1022    D.: Global Carbon Budget 2017, Earth Syst. Sci. Data Discuss., 2017, 1-79, 2017.

1023    Machta, L. and Hughes, E.: Atmospheric Oxygen in 1967 to 1970, Science, 168, 3939, 1582-1584,

1024    1970.

1025  Manning, A.: Temporal variability of atmospheric oxygen from both continuos and measurements

1026  and a flask sampling network: tools for studying the global carbon cycle, Ph.D. Ph.D., University of

1027  California, San Diego, San Diego, Calofornia, USA, 2001.

1028  Manning, A. C. and Keeling, R. F.: Global oceanic and land biotic carbon sinks from the Scripps

1029  atmospheric oxygen flask sampling network, Tellus B, 58, 95-116, 2006.

1030  Manning, A. C., Keeling, R. F., and Severinghaus, J. P.: Precise atmospheric oxygen measurements

1031  with a paramagnetic oxygen analyzer, Global Biogeochem Cy, 13, 1107-1115, 1999.

1032  Marrero, T. R. and Mason, E. A.: Gaseous Diffusion Coefficients, Journal of Physical and Chemical

1033  Reference Data 1, 3, 1972.

1034  Martin, N. A., Ferracci, V., Cassidy, N., and Hoffnagle, J. A. J. A. P. B.: The application of a cavity ring-

1035  down spectrometer to measurements of ambient ammonia using traceable primary standard gas

1036  mixtures, 122, 219, 2016.

1037  Mckay, L. F., Eastwood, M. A., and Brydon, W. G.: Methane Excretion in Man - a Study of Breath,

1038  Flatus, and Feces, Gut, 26, 69-74, 1985.

1039  Nevison, C. D., Keeling, R. F., Kahru, M., Manizza, M., Mitchell, B. G., and Cassar, N.: Estimating net

1040  community production in the Southern Ocean based on atmospheric potential oxygen and satellite

1041  ocean color data, Global Biogeochem Cy, 26, 2012.

1042  Oney, B., Henne, S., Gruber, N., Leuenberger, M., Bamberger, I., Eugster, W., and Brunner, D.: The

1043  CarboCount CH sites: characterization of a dense greenhouse gas observation network, Atmos.

1044  Chem. Phys., 15, 11147-11164, 2015.

1045  Press, W. H., Teukolsky, S. A., Vetterling, W. T., and Flannery, B. P.: Numerical Recipes 3rd Edition:

1046  The Art of Scientific Computing, Cambridge Printing Press, Cambridge, England, 1986.

1047  Press, W. H., Teukolsky, S. A., Vetterling, W. T., and Flannery, B. P.: Numerical recipes in C: the art of

1048  scientific computing, Cambridge University Press, London, 1992.

1049  Ryter, S. W. and Choi, A. M. K.: Carbon monoxide in exhaled breath testing and therapeutics, J Breath

1050  Res, 7, 2013.

1051  Satar, E., Berhanu, T. A., Brunner, D., Henne, S., and Leuenberger, M.: Continuous CO2/CH4/CO

1052  measurements (2012–2014) at Beromünster tall tower station in Switzerland, Biogeosciences, 13,

1053  2623-2635, 2016.

1054  Schibig, M. F., Steinbacher, M., Buchmann, B., van der Laan-Luijkx, I. T., van der Laan, S., Ranjan, S.

1055  and Leuenberger, M. C,: Comparison of continuous in situ CO2 observations at Jungfraujoch using

1056  two different measurement techniques, Atmospheric Measurement Techniques

1057  , 8, 57-68, 10.5194/amt-8-57-2015, 2015.

1058  Severinghaus, J. P.: Studies of the terresterial O2 and carbon cycles in sand dune gases and in

1059  Biosphere Doctoral Ph.D., Columbia University, New York, USA, 1995.

1060  Steig, E. J., Gkinis, V., Schauer, A. J., Schoenemann, S. W., Samek, K., Hoffnagle, J., Dennis, K. J., and

1061  Tan, S. M.: Calibrated high-precision $^{17}$O-excess measurements using cavity ring-down

1062  spectroscopy with laser-current-tuned cavity resonance, Atmos. Meas. Tech., 7, 2014.

1063  Stephens, B. B., Bakwin, P. S., Tans, P. P., Teclaw, R. M., and Baumann, D. D.: Application of a

1064  differential fuel-cell analyzer for measuring atmospheric oxygen variations, J Atmos Ocean Tech, 24,

1065  82-94, 2007.

1066  Sturm, P., Leuenberger, M., Valentino, F.L., Lehmann, B. and B. Ihly: Measurements of $CO_2$, its stable

1067  isotopes, $O_2/N_2$, and $^{222}$Rn at Bern, Switzerland, *Atmospheric Chemistry and Physics*, *6*, 1991-2004,

1068  2006.

1069  Tan, Y., Kochanov, R.V., Rothman, L., and Gordon, I.E.:Introduction of water-vapor broadening

1070  coefficients and their temeprature dependence exponents into the HITRAN database, Part 1: CO2,

1071  N2O, CO, CH4, O2, NH3, and H2S, Submitted to Journal of Geophysical Research Atmospheres, 2019,

1072  arXiv:1906.01475 .

1073 Tennyson, J., Bernath, P. F., Campargue, A., Császár, A. G., Daumont, L., Gamache, R. R., Hodges, J. T.,

1074 Lisak, D., Naumenko, O. V., Rothman, L. S., Tran, H., Zobov, N. F., Buldyreva, J., Boone, C. D., De Vizia,

1075 M. D., Gianfrani, L., Hartmann, J.-M., McPheat, R., Weidmann, D., Murray, J., Ngo, N. H., and

1076 Polyansky, O. L.: Recommended isolated-line profile for representing high-resolution spectroscopic

1077 transitions (IUPAC Technical Report), 86, 1931–1943, 2014.

1078 Tohjima, Y.: Method for measuring changes in the atmospheric O-2/N-2 ratio by a gas

1079 chromatograph equipped with a thermal conductivity detector, J Geophys Res-Atmos, 105, 14575-

1080 14584, 2000.

1081 Tran, H., Turbet, M., Hanoufa, S., Landsheere, X., Chelin, P., Ma, Q., Hartmann, J.: The $CO_2$–

1082 broadened $H_2O$ continuum in the 100–1500 cm-1 region: Measurements, predictions and empirical

1083 model, Journal of Quantitative Spectroscopy and Radiative Transfer, 230, 75-80, 2019.

1084 Valentino, F. L., Leuenberger, M., Uglietti, C., and Sturm, P.: Measurements and trend analysis of O2,

1085 CO2 and δ13C of CO2 from the high altitude research station Junfgraujoch, Switzerland — A

1086 comparison with the observations from the remote site Puy de Dôme, France, Sci Total Environ, 391,

1087 203-210, 2008.

1088 Varghese, P. L. and Hanson, R. K.: Collisional narrowing effects on spectral line shapes measured at

1089 high resolution, Appl. Opt., 23, 2376-2385, 1984.

1090 Wójtewicz, S., Cygan, A., Masłowski, P., Domysławska, J., Wcisło, P., Zaborowski, M., Lisak, D.,

1091 Trawiński, R. S., and Ciuryło, R.: Spectral line-shapes of oxygen B-band transitions measured with

1092 cavity ring-down spectroscopy, Journal of Physics: Conference Series, 548, 012028, 2014.

1093 Wolf, P. G., Parthasarathy, G., Chen, J., O'Connor, H. M., Chia, N., Bharucha, A. E., and Gaskins, H. R.:

1094 Assessing the colonic microbiome, hydrogenogenic and hydrogenotrophic genes, transit and breath

1095 methane in constipation, Neurogastroent Motil, 29, 2017.

1096    Zellweger, C., Forrer, J., Hofer, P., Nyeki, S., Schwarzenbach, B., Weingartner, E., Ammann, M., and

1097    Baltensperger, U.: Partitioning of reactive nitrogen ($NO_y$) and dependence on

1098    meteorological conditions in the lower free troposphere, Atmos. Chem. Phys., 3, 779-796, 2003.

1099